Numerical Analysis of Aerodynamic Characteristics of Multi-Pod Hyperloop System

Written by:

Muhammad Omer Mirza

Reg. # 00000330212

Project Supervisor:

Dr. Zaib Ali

Assistant Professor

School of Mechanical and Manufacturing Engineering

National University of Sciences and Technology, Islamabad

June 21, 2022

Numerical Analysis of Aerodynamic Characteristics of Multi-Pod Hyperloop System

Author

Muhammad Omer Mirza

Registration Number

330212

A thesis submitted in partial fulfillment of the requirements for the degree of

MS Mechanical Engineering

Thesis Supervisor:

Dr. Zaib Ali

Thesis Supervisor's Signature: _____

DEPARTMENT OF MECHANICAL ENGINEERING

SCHOOL OF MECHANICAL & MANUFACTURING ENGINEERING

NATIONAL UNIVERSITY OF SCIENCES AND TECHNOLOGY,

ISLAMABAD

Declaration

I certify that this research work titled *"Numerical Analysis of Aerodynamic Characteristics of Multi-Pod Hyperloop System"* is my own work. The work has not been presented elsewhere for assessment. The material that has been used from other sources it has been properly acknowledged/referred.

Signature of Student

Muhammad Omer Mirza

2020-NUST-MS-MECH-330212

Plagiarism Certificate (Turnitin Report)

This thesis has been checked for Plagiarism. Turnitin report endorsed by Supervisor is attached.

Signature of Student

Muhammad Omer Mirza

Registration Number: 330212

Signature of Supervisor

Thesis Acceptance Certificate

Certified that final copy of MS thesis written by **Muhammad Omer Mirza** Registration No. **00000330212** of SMME has been vetted by undersigned, found complete in all aspects as per NUST Statutes/Regulations, is free of plagiarism, errors, and mistakes and is accepted as partial fulfillment for award of MS/MPhil degree. It is further certified that necessary amendments as pointed out by GEC members of the scholar have also been incorporated in the said thesis.

Signature with stamp:

Name of Supervisor: Dr. Zaib Ali

Date: _____

Signature of HOD with Stamp:

Date: _____

Countersign by:

Signature

(Dean/Principle):

Date: _____

FORM TH-4

MASTER THESIS WORK

We hereby recommend that the dissertation prepared under our supervision by: **Muhammad Omer Mirza (00000330212)**, Titled: "**Numerical Analysis of Aerodynamic Characteristics of Multi-Pod Hyperloop System**" be accepted in partial fulfillment of the requirements for the award of **MS Mechanical** degree.

Examination Committee Members

1. Name: Dr. Emad Ud Deen Signature: _____

2. Name: Dr. Adnan Munir Signature: _____

3. Name: Dr. Niaz Bahadur Signature: _____

Supervisor's name: Dr. Zaib Ali Signature: _____

_____ _____

Head of Department Date

COUNTERSINGED

_____

Dean/Principal

Date: _____

Copyright Statement

Acknowledgements

I am thankful to my Creator Allah Subhana-Watala to have guided me throughout this work at every step and for every new thought which You setup in my mind to improve it. Indeed I could have done nothing without Your priceless help and guidance. Whosoever helped me throughout the course of my thesis, whether my parents or any other individual was Your will, so indeed none be worthy of praise but You.

I am profusely thankful to my beloved parents who raised me when I was not capable of walking and continued to support me throughout in every department of my life.

I would also like to express special thanks to my supervisor Assistant Professor “Dr Zaib Ali” for his help throughout my thesis and also for the Optimization of Energy System course which he has taught me. I can safely say that I haven't learned any other engineering subject in such depth than the ones which he has taught.

I would also like to thank Dr. Emad Uddin, Dr. Adnan Munir, and Dr Niaz Bahadur Khan for being on my thesis guidance and evaluation committee.

Finally, I would like to express my gratitude to all the individuals who have rendered valuable assistance to my study.

Dedicated to my exceptional parents and adored siblings whose tremendous support and cooperation led me to this wonderful accomplishmet.

Abstract:

The Hyperloop system is a new and innovative mode of transportation, in which high-speed pods move through near-vacuum tubes. In this study, a multi-pod Hyperloop system was analyzed using numerical simulations at different values of distance between the pods (i.e., 2L to 4L). The numerical simulations were conducted using an unsteady, compressible solver with the Reynolds-average Naiver Stokes model to determine the effect of distance between the pods on the aerodynamic characteristics and pressure wave behaviour in the Hyperloop system. Moreover, the aerodynamic drag and pressure wave characteristics were determined theoretically based on the quasi-one-dimensional conditions to compare them to the numerical results. The flow conditions around the pods were divided into three different flow regimes based on the speed of the pods. In the flow regime 1 ($v_{pod} = 100\, m/s$), the compression waves develop into normal shock waves for the second pod without the occurrence of the choking of the flow at the throat. However, no shock wave occurs for the first pod due to the interaction of the low-pressure expansion wave and high-pressure compression wave at the tail of the first pod. Moreover, increasing the distance between the pods results in smoothening of the pressure distribution around the pods. In the flow regime 2 ($v_{pod} = 200\, m/s$), choking happens at the throat of the second pod and an oblique shock wave starts to appear within the tail section of the pod. Moreover, no chocking is observed for the tail section of the first pod, due to the low-pressure expansion wave and high-pressure compression wave between the two pods. Increasing the distance between the pods delays the interaction of the two waves, but overall due to the high-pressure value at the tail of the first pod, no shockwave phenomenon is observed. In the flow regime 3 ($v_{pod} = 300 - 400\, m/s$), the oblique shock wave at the tail of the second pod is swept to the larger length and finally achieves a constant pressure value. Whereas an oblique

shock wave starts to appear at the tail section of the first pod. Another major change that is observed is the decrease in the drag force value with the increase in the distance between the pods at all pod speeds. Increasing the distance between the pods results in smooth interaction between the trailing oblique shock wave of the first pod and the leading normal shock wave of the second pod. This results in a lower pressure value at the tail end of the first pod and at the head of the second pod, which results in a low value of pressure difference between the head and tail sections of the pods and hence, a decrease in the total drag value. Based on this study, it is found that increasing the distance between the pods delays the pressure waves interaction which in turn results in a decrease in the total drag value.

Table of Contents

List of Figures

List of Tables

Chapter No. 1

This chapter deals with the introduction and literature review to the Hyperloop System. The Hyperloop System is an innovative mode of transportation that includes the pods that travel through near-vacuum tubes. The lower pressure value allows the pods to move at high speeds i.e., sonic, and hypersonic. The detailed introduction along with the innovations that could be applied to this technology are presented in this chapter.

1. Introduction:

Numerous industries place a premium on environmental stewardship. This is owing to the depletion of natural resources, but it also has marketing, public relations, and cost advantages. The transportation industry is one of these areas that is motivating and trying to become more environmentally friendly.

The negative consequences of transportation on the environment are causing major concerns around the world, mostly because of the ever-expanding travel networks and advances within this sector, which have been spurred by the continually increasing demand for linked, high-speed travel. It is predicted that by 2050, high-speed transport would account for 41% of the global transportation market share, according to one estimate[1]. Regulatory authorities will be required to develop rules and regulations that will grow stricter by the decade, to reduce noise and greenhouse gas emissions because of the use of nonrenewable energy sources. A new mode of transportation that complies with these requirements and regulations is required because of the above as well as the growing need for high-speed transit.

Hyperloop is an evacuated tube maglev train (ETMT) technology suggested by Elon Musk in response to recent technological developments and the growing need for affordable transportation[2-5]. Passengers would be transported in a maglev pod via a near-vacuum tunnel (1/1000 atm.) at transonic speeds. A combination of low tube pressure and maglev technology reduces the aerodynamic drag induced by high operating speeds[6, 7]. When compared to traditional transportation systems, the Hyperloop is a novel transportation mode that can comply with these requirements while also demonstrating considerable advantages. The technology consists of passenger pods that are driven via a tunnel in which the pressure is dropped to 0.1-1%

of the surrounding atmosphere[8] before reaching their destination. As a result of the lower pressure, the density is likewise reduced for the same temperature. Because of the low density, the pods endure a reduced level of aerodynamic drag. To achieve the planned operating velocity of 600 mph, the pods are levitated by electromagnets while being pushed by a magnetic linear accelerator.

The transportation mechanism of the Hyperloop is very much like that of a train, even though it is supposed to be a straight "A-to-B" link. Having both a fast-operating speed (Ma = 0.88) and great energy efficiency is a common design challenge in the aerospace industry. A hybrid of rail and air transportation, it utilizes ground transportation as well as aircraft technology to achieve a whole new level of performance. Emissions are reduced when travelling at aero plane speeds in a high-capacity transportation mode. It also covers NASA's research objectives for high-speed transportation, including demand growth, sustainability, and technological convergence[9].

Moreover, the fluid (air) inside the tube is compressed due to the high-speed relative motion between the pod and tube walls which causes intense friction, this results in aerodynamic heating or aerothermal phenomenon[10]. The rise in the temperature value inside the tube results in deterioration of the thermal environment[11, 12]. Additionally, when the pod inside the tube runs at or above the speed of sound, the aerodynamic effects inside the tube are aggravated, which results in the formation of shock waves inside the tube. The formation of the shock waves deteriorates the flow and heat transfer process inside the tube[13, 14]. It may also result in fatigue damage to the structure of the pod and tube. This demands the study of the shock waves and defining the minimum distance between the pods if multiple pods are running inside the same tube.

The existence of the multiple pods inside the tube causes the flow stream to vary in front as well as behind the pods (i.e., at the nose and tail of the pods). Moreover, the interaction between the leading shock wave of the second pod and the trailing oblique shock wave of the first pod is inevitable based on the distance value between the pods. The interaction of the two waves causes the fluctuation of the aerodynamic properties (i.e., pressure, velocity, and temperature). These studies are aimed at advancing Hyperloop technology by determining the appropriate distance between pods, which will help reduce aerodynamic drag, and by examining flow patterns surrounding each pod. The interaction of the leading shock wave of the second pod and the trailing oblique shock wave of the first pod is observed for this research work. The aerodynamic characteristics are studied by varying the distance between the pods. The variation of pressure, Mach number and temperature are studied for both pods, at the tail of the first pod and the head of the second pod.

Chapter No. 2

This section provides the literature review to the Hyperloop System. Comprehensive literature analysis was carried out to understand the working of the Hyperloop System as well as to find the point that will contribute towards the better understanding as well as for the development of this technology. It was found that the aerodynamic characteristic of the pods is highly dependent on the pressure, speed, temperature, and other parameters. All these parameters and the work that has already been completed is described in this chapter.

2. Literature Review:

An object that is travelling at high speed (i.e., $Ma \approx 1$), results in variation in the pressure field. Moreover, travelling of a high-speed object in a confined space (i.e., high speed train inside a tunnel), the compression of the flow in the frontal region of the object causes chocking phenomenon to occur. The theoretical and experimental studies related to high-speed projectile motion inside a tube show the generation and propagation of compression waves and expansion waves inside the tube[15]. Increasing the speed of the objective to the critical value results in the generation of an oblique shock wave and a trailing shock wave behind the projectile. Assorted studies show that the aerodynamic characteristics changes as the object move inside the tube, and these variations are a function of the speed of the object as well as the diameter ratio of the object and the tube (i.e., blockage ratio). Moreover, the transition in the aerodynamic properties is amplified when the speed of the object reaches the transonic speeds[15, 16].

The main objective of the researchers for the Hyperloop system is to reduce the aerodynamic drag value, which will result in economic efficiency and feasibility of high-speed trains/pods. The aerodynamic properties of the Hyperloop system are studied by various researchers by changing the speed of the pod[7, 17-21], the pressure inside the tube[7, 17-19, 21], the shape of the pod[17, 22], the variation of the blockage ratio (i.e. which is the ratio of the cross-sectional area of the pod to the cross-sectional area of the tube)[18-20], and the length of the tube[7]. Increasing the speed of the pod or pressure of the tube or blockage ratio (BR) or length of the pod results in an increase in the value of aerodynamic drag value and vice versa.

Previous studies have studied the generation and effects of the leading shock wave (compression wave) and oblique shock wave (trailing shock wave) behind the pod. Both the compression wave and the oblique shock wave become stronger with the increase in the value of the speed of the pod, the blockage ratio (BR), and the decrease in the temperature inside the tube. The study of the generation of this shockwave has been conducted under steady-state conditions as well as under unsteady conditions[7, 16-21, 23]. However, the propagation of the pressure waves cannot be studied under steady-state conditions. Moreover, the reflection of the pressure waves from the boundary of the computational domain has an adverse effect on the results of the simulation[16].

The unsteady simulations previously conducted on the Hyperloop system show that the total drag increases with the increase in the strength of the oblique shock wave[24]. The effect of the variation of the pod speed[12, 24], the pressure inside the tube[24], the blockage ratio (BR)[24, 25], and the shape of the pod[14] have also been studied by previous researchers. Moreover, the generation and properties of the oblique shock wave during the acceleration and deceleration of the pod have also been studied[26], along with the generation of different types of pressure waves has been thoroughly studied by various researchers[16]. However, the effects due of the interaction of the trailing shock wave of the leading pod and the leading shockwave of the trailing pod have not been considered previously.

It has been studied previously that the compression wave, expansion wave, and oblique shock wave affect the aerodynamic characteristics of the pod inside the tube[24, 27]. The flow regime in front of the pod changes due to the existence of the compression wave in front of it. Similarly, the flow regime behind the pod is also disturbed due to the existence of the oblique shockwave. Moreover, the compression wave can propagate faster than the speed of sound while

the expansion waves in the downstream region prolongate at the speed of sound[28]. Recently, different studies have been conducted by the various researcher regarding the compression waves, expansion waves and oblique shock waves, and how these pressure waves affect the aerodynamic characteristics of the pod inside the tube[13, 25, 29]. Moreover, it has also been found that the normal shock wave relation applies to the Hyperloop system, and these relationships are applied to the Hyperloop numerical system by *Jang et al*.[16]. However, the effect of the interaction of the pressure waves on the aerodynamic characteristics of the Hyperloop system and the optimal distance between multiple pods inside the same vacuum tube has not been analyzed.

The development of the shock waves inside the tube plays a vital role in determining the aerodynamic characteristics of the Hyperloop system. Previous studies have analyzed the effect of shock waves on the temperature and pressure distribution inside the tube. The focus was to study the variation of the temperature and pressure value close to the pod and tube walls. The studies conducted by *Niu et al*. confirm that the existence of shock waves endangers the structural integrity of the pod and has an adverse effect on the environment inside the tube[12, 25]. The studies on the influence of the blockage ratio on aerothermal effects inside the tube suggest that the deterioration of the environment happens because shockwaves are affected by the BR value[25].

The understanding of the compressible flow phenomenon helps to analyze the aerodynamic characteristics of the single pod Hyperloop system. The flow regime, as well as the pressure wave distribution in different flow regimes, have been studied by *Jang et al.* and based on the pressure distribution the effect of the pressure wave on the aerodynamic drag has been analyzed[16]. However, the existence of multiple pods inside the same tube has not been studied

yet. Moreover, the existence of the multiple pods inside the same tube effects the pressure wave distribution of each pod and hence results in a change in the aerodynamic characteristics of the pods. Therefore, there should be an optimal distance between the pods so that the flow regime of one pod does not affect the flow regime of the other pod. This study will deal with the pressure wave distribution as well as the aerodynamic characteristics of the two pod Hyperloop system at different distances from each other. The distance between the pods will be varied to study the pressure wave distribution as well as the change in the aerodynamic drag on the pods.

Chapter No. 3

This chapter describes the methodology that will be utilized to carry out this research work. The numerical simulation is conducted via ANSYS Fluent. The geometrical configuration, parameters defined for the meshing, the domain of the numerical model, and the boundary conditions applied to the designed model are described in this chapter.

3. Methodology:

3.1. Theoretical Consideration:

The flow properties for the given numerical simulation are assumed to be in-viscous and isentropic. However, these assumptions are not valid across the normal shock waves. According to [16, 30, 31], a quasi-one-dimensional flow is also assumed through the Hyperloop System due to its similarities to the flow through the converging-diverging nozzle and, because this method is adequate for capturing the key flow characteristics. The shape of the pods and tube used for the simulation are presented in Fig.

3.2. Assumptions and Governing Equations:

It is necessary to make assumptions and simplify the aerodynamic model to lower the complexity of the model and, as a result, the computing effort required. It is clear, however, that the physical aspects must still be accurately represented, which implies that caution must be taken while constructing these simplifications in the first place. Because of this, it is critical to validate the model using CFD to determine whether the model can simulate the physical situation and to determine which of the neglected effects are responsible for any potential but acceptable inconsistencies.

Initial modelling of flow around a pod involves simulating the flow via a channel with a variable area, with the pod surface and tube wall acting as channel walls. So, the flow domain may be thought of as a compressible (convergent-divergent) nozzle, with the assumption that there will be a minimum section somewhere on or near the pod surface, which corresponds to the throat of the section. The assumption is further strengthened by assuming that the change in area is gradual, resulting in the flow being modelled as a quasi-1D flow. This kind of flow is

characterized by the fact that all significant flow parameters change in a single direction, which in this instance is the flow in the x-direction. The following are the most significant implications of this premise, in order of importance:

Furthermore, it is assumed that the flow is isentropic. The idealization of isentropic flow is usually considered to be a realistic approximation of the actual flow behaviour for accelerating flows (favorable pressure gradients), according to [32]. Moreover, this provides support for the isentropic flow assumption since the flow around the pod is in an accelerating condition for a considerable portion of its length in interest. The isentropic flow assumption is primarily based on the assumption that certain parameters, such as the total temperature, remain constant across the flow domain throughout the flow domain.

- The flow parameters are uniform along each section i.e., $A = A(x), p = p(x)$ etc.
- $V_x \neq 0$
- $\frac{V_y}{V_x} \ll 0$
- $\frac{V_z}{V_x} \ll 0$

Moreover, the flow is steady in nature and inviscid, and the air is assumed to act as an ideal gas. According to this assumption, the heat capacity ratio γ for air is equal to 1.4 and the ideal gas law is acceptable for calculating purposes. The quasi-1D flow assumption has ramifications for the fluid dynamic equations that regulate fluid motion. The next subsections will provide a brief discussion of how these equations relate to the flow field under examination in general.

3.2.1. Mathematical Modelling:

The governing equations for the case of compressible flow problems are the conservation of mass (Equation of Continuity), conservation of momentum (Navier-Stokes Equations), and the equation for the conservation of energy. The mathematical description for the conservation of mass is represented as follows:

$$\frac{\partial \rho}{\partial t} + \frac{\partial (\rho u_i)}{\partial x_i} = 0 \tag{1}$$

The general equation defined for the conservation of mass applies to both the incompressible flow as well as to the compressible flow[33]. Similarly, the general equations for the conservation of momentum and energy are defined as follows:

$$\frac{\partial (\rho u_i)}{\partial t} + \frac{\partial \left(\rho u_i u_j\right)}{\partial x_i} = -\frac{\partial P}{\partial x_i} + \frac{\partial}{\partial x_j}\left[\mu\left(\frac{\partial u_i}{\partial x_i} + \frac{\partial u_j}{\partial x_j} - \frac{2}{3}\delta_{ij}\frac{\partial u_k}{\partial x_k}\right)\right] + \frac{\partial}{\partial x_j}\left(-\rho\{u_i' u_j'\}\right) \tag{2}$$

$$\frac{\partial (\rho E)}{\partial t} + \frac{\partial \left(u_j(\rho E + P)\right)}{\partial x_i} = \frac{\partial}{\partial x_j}\left[\mu_i \mu_{eff}\left(\frac{\partial u_i}{\partial x_i} + \frac{\partial u_j}{\partial x_j} - \frac{2}{3}\delta_{ij}\frac{\partial u_k}{\partial x_k}\right)\right] + \frac{\partial}{\partial x_j}\left[\left(-k_{eff}\right)\frac{\partial T}{\partial x_j}\right] \tag{3}$$

Where the factors ρ, u, p, and μ are the fluid density, fluid velocity, fluid pressure, and fluid viscosity, respectively. Similarly, the terms like E, k_{eff} and μ_{eff} in the energy equation are the specific internal energy, the effective thermal conductivity, and the effective dynamic

viscosity, respectively[33]. In addition to all these equations, the solver employed for the modelling of the mathematical simulation was the SST $k-\ \omega$ turbulence model.

3.2.2. SST k- ω Turbulence Model:

One of the most implicated turbulence models is the SST $k-\ \omega$ turbulence model. This turbulence model is a two-equation eddy viscosity model. The main advantage of this model is that it combines two of the best turbulence models i.e. $k-\omega$ and $k-\varepsilon$ models [34]. The central region of the computational domain is solved by $k-\omega$ while the boundary layer region is solved by $k-\varepsilon$. This model can flip to $k-\varepsilon$ behaviour in the free stream, avoiding the typical problems encountered with the $k-\omega$ model. However, there is some evidence that the SST $k-\omega$ model produces somewhat excessive turbulence levels in areas with high normal strain, such as stagnation regions and regions with considerable acceleration[35]. Moreover, the tendency to produce error is far less prominent ass compared to the typical $k-\omega$ and $k-\varepsilon$ model. The governing equation for the SST $k-\omega$ model is[36]:

Turbulence Kinetic Energy:

$$\frac{\partial k}{\partial t}+U_j\frac{\partial k}{\partial x_j}=P_k-\beta^*k\omega+\frac{\partial}{\partial x_j}\left[(v+\sigma_k v_T)\frac{\partial k}{\partial x_j}\right] \tag{4}$$

Specific Dissipation Rate:

$$\frac{\partial \omega}{\partial t}+U_j\frac{\partial \omega}{\partial x_j}=\alpha S^2-\beta\omega^2+\frac{\partial}{\partial x_j}\left[(v+\sigma_\omega v_T)\frac{\partial \omega}{\partial x_j}\right]+2(1-F_1)\sigma_{\omega^2}\frac{1}{\omega}\frac{\partial k}{\partial x_i}\frac{\partial \omega}{\partial x_i} \tag{5}$$

F_1 (Blending Function):

$$F_1 = \tanh\left\{\left\{\min\left[\max\left(\frac{\sqrt{k}}{\beta^*\omega y'}\frac{500v}{y^2\omega}\right), \frac{4\sigma_{\omega^2}k}{CD_{k\omega}y^2}\right]\right\}^4\right\} \quad (6)$$

Note: $F_1 = 1$ inside the boundary layer and 0 in the free stream[36].

Kinematic eddy viscosity:

$$v_T = \frac{\alpha_1 k}{\max(\alpha_1\omega, SF_2)} \quad (7)$$

F_2 (Second Blending Function):

$$F_2 = \tanh\left[\left[\max\left(\frac{2\sqrt{k}}{\beta^*\omega y'}\frac{500v}{y^2\omega}\right)\right]^2\right] \quad (8)$$

P_k (Production Limiter):

$$P_k = \min\left(\tau_{ij}\frac{\partial U_i}{\partial x_j}, 10\beta^* k\omega\right) \quad (9)$$

Based on its greater accuracy, the SST $k-\omega$ turbulence model has been employed to study the aerodynamic behaviour of the Multi-Pod Hyperloop System[33, 36-38].

3.2.3. Converging Diverging Nozzle Assumptions:

The flow inside the tube of the Hyperloop System undergoes a variation like the flow inside the converging-diverging nozzle. The only difference between the two systems is that the

fluid moves inside the converging-diverging nozzle while in the case of the Hyperloop system, the pods are moving, and the flow field changes around them. The equations used to predict the local change in the flow field across the leading shock wave are described below:

$$\frac{P_b}{P_a} = \frac{2\gamma(M_a^s)^2 - (\gamma - 1)}{\gamma + 1} \tag{10}$$

$$\frac{\rho_b}{\rho_a} = \frac{(\gamma + 1)(M_a^s)^2}{(\gamma - 1)(M_a^s)^2 + 2} \tag{11}$$

$$\frac{T_b}{T_a} = \frac{[(\gamma - 1)(M_a^s)^2 + 2][2\gamma(M_a^s)^2 - (\gamma - 1)]}{(\gamma + 1)^2(M_a^s)^2} \tag{12}$$

$$M_b^s = \sqrt{\frac{(\gamma - 1)(M_a^s)^2 + 2}{2\gamma(M_a^s)^2 - (\gamma - 1)}} \tag{13}$$

Moreover,

$$M_a^s = \frac{v_a^s}{\sqrt{\gamma R T_a}} \tag{14}$$

$$M_b^s = \frac{v_b^s}{\sqrt{\gamma R T_b}} \tag{15}$$

The P and ρ are the pressure and density of the fluid, respectively. Similarly, the Mach number for point b is calculated from the following equation.

$$M_a^p = \frac{M_{LSW}\left[(\gamma + 1)M_{pod} - 2M_{LSW}\right] + 2}{\sqrt{[2\gamma(M_{LSW})^2 - (\gamma - 1)][(\gamma - 1)(M_{LSW})^2 + 2}} \tag{16}$$

Were

$$M_{pod} = \frac{-v_{pod}}{\sqrt{\gamma R T_a}} \tag{17}$$

These equations are solved to get the value of M_{pod}. The values of the parameters like γ, A_t and A_{pod} are already known from the initial assumption of the model.

3.3. Computational Domain:

The boundary conditions applied to the computational domain are shown in Figure. The shape of the pod is one of the most important parameters because it affects the aerodynamic characteristics of the pod. Different shapes of the pod have been studied in previous studies to reduce the aerodynamic drag on the pod[18, 39-41]. The most ideal pod shape has been used for both pods in this study. The hemispherical shape is applied to the nose and tail of both pods to study the general shock wave and aerodynamic characteristics in between the pods. The aerodynamic characteristics were studied throughout the pod's length. The pod had a dimeter of 3 m, and the remaining section had a length of 40 m. The diameter of the tube was set to be 5 m along with a blockage ratio of 0.36 in all the simulations. The length of the tube varies with the distance between the pods (i.e., 430, 451.5, 473, 494.5, and 516 m for the distance value of 2L, 2.5L, 3L, 3.5L, and 4L, respectively between the pods). The inflow and outflow domain are kept small in all the simulations because the aerodynamic characteristics at the tail of the first pod and the nose of the second pod were studied.

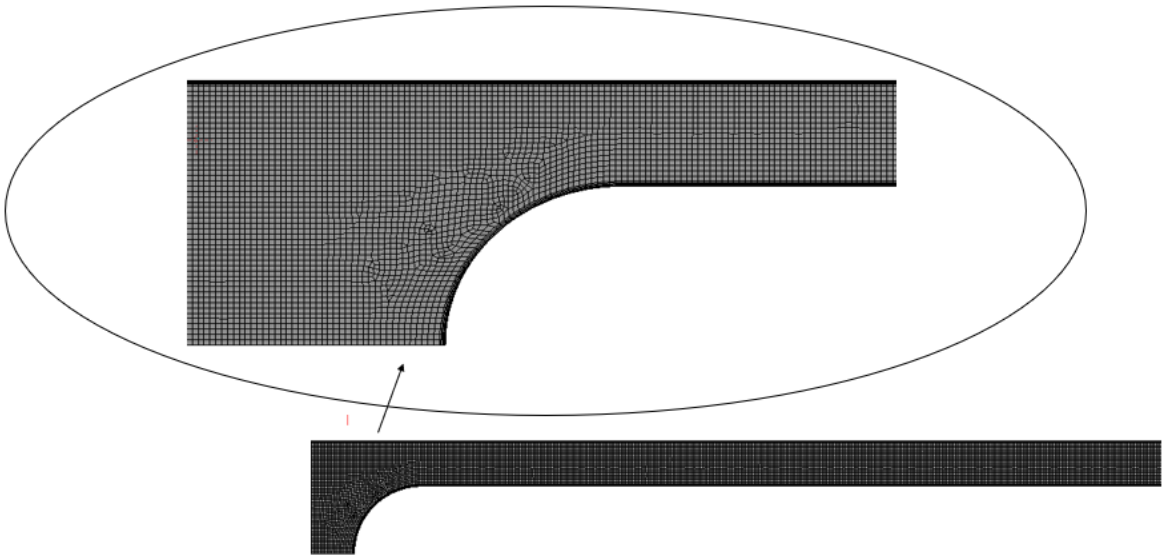

Figure 1: Mesh Distribution around the pods

Like a converging-diverging nozzle, the flow inside the tube of the Hyperloop System encounters the change in the cross-sectional area. The converging and diverging sections are observed at the head and tail of the pods inside the tube. Based on this, for the given analysis, the convergent section is defined for the area between the tube and the head of the pods, whereas the divergent is defined for the area between the tube and the tail of the pods. Moreover, the cross-sectional area through the straight section of the pods remains the same, as seen in the figure. This results in the development of the boundary layers due to the viscous effects along the length of the pod and tube walls. As the thickness of these boundary layers increases (i.e., the area between the tube and pods wall converges) the flow is accelerated between the pod and tube wall. As a result, the flow cross-sectional area converges through the straight section of the tube in a way like Fanon Flow. Since the thickness of the developed boundary layer is maximum at the end of the straight, a region like the throat section of the converging-diverging nozzle is developed at the end of the straight section, as seen in the figure.

All the numerical simulations were tested in ANSYS Fluent 2020 R1. Under the unsteady state conditions, a two-dimensional, axisymmetric, compressible flow model was solved using a density-based solver in this study. The unsteady simulation allows for economically efficient modelling with adequate accuracy[7] along with the investigation of pressure wave propagation[15, 17, 42]. The solver employed is the implicit Roe's flow difference for the spatial discretization of the governing equations[43-45]. The least-squares cell-based method was used to find the gradient term. For the discretization of the flow terms, turbulence kinetic energy, and specific dissipation rate the second-order upwind approach was used. For the time integration, the implicit first-order method is utilized. The air was assumed to be an ideal gas along with Sutherland's law to define its viscosity value. Because the Reynolds number lies within the range of turbulence regime, it is suitable to employ a proper turbulence model to predict the turbulence effect. It is possible to correctly model the mechanics of complex flow motion using direct numerical simulation and large eddy simulation; however, the processing cost is too high[16, 46-50]. The shear stress transport (SST) $k-\omega$ viscous model was employed because the flow employs both the laminar region and turbulence along with lower computational cost. Moreover, the accuracy of SST $k-\omega$ is more as compared to the simple $k-\omega$ and $k-\varepsilon$ model because it employs the combination of the two models.

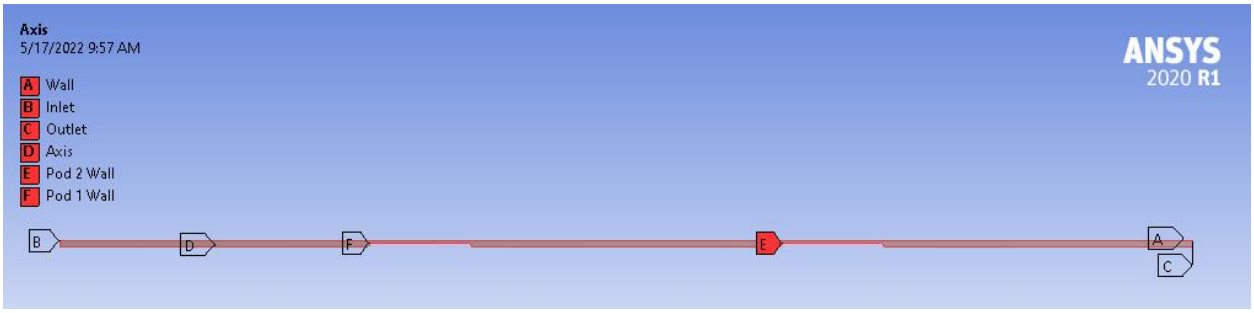

Figure 2: Schematic of the boundary conditions applied to the Multi-Pod Hyperloop System

The boundary condition applied to the inlet of the domain was pressure far-field because it is non-reflecting for one-dimensional flow. The speed of incoming flow was set to be 100, 200, 300, and 400 m/s (Ma = 0.2881, 0.5762, 0.8643, and 1.152, respectively) to study the aerodynamic characteristics of the pods. For this purpose, the walls of the tube were set to motion. Whereas the boundary condition applied to the pods wall was a no-slip boundary condition. The pressure value was set to be 101.325 Pa at the inlet along with the temperature value of 300 K for all the simulations. The distance between the pods varied from 2L to 4L for an increment of 0.5L for each case (i.e., 2L, 2.5L, 3L, 3.5L and 4L, respectively). In this way, five different models with varying lengths of the tube were studied. At the outlet of the domain, the pressure outlet boundary condition was defined. The reference frame was defined in such a way that it moves with the same speed as that of the pods.

3.4. Computational Grid:

The mesh was drawn using ANSYS mechanical. Because of the symmetrical nature of the configurations, the numerical domain was set to be two dimensional and axisymmetric. The quadrilateral mesh was defined throughout the length of the tube. Moreover, inflation layers were defined at the walls of the pod as well as on the inner wall of the tube. This is because the development of the boundary layers plays a vital role in the development of shock waves. The mesh size was set to be 0.01 m for the simulations, the y+ value distribution around the pods is shown in Figure 1. For the mesh independence test, the velocity value of 400 m/s along with the pressure value of 101.325 Pa was selected. The results of the mesh independence test are presented in Table 1.

Table 1: Detailed parameters of the grid independence test

Case	Mesh Type	Pressure of leading shock wave	Aerodynamic Drag on the 1st Pod	Aerodynamic Drag on the 2nd Pod
1	Coarse	263.963	1444.1885	1255.5349
2	Medium	261.638	1347.1699	1205.0811
3	Fine	258.463	1274.2622	1132.4538

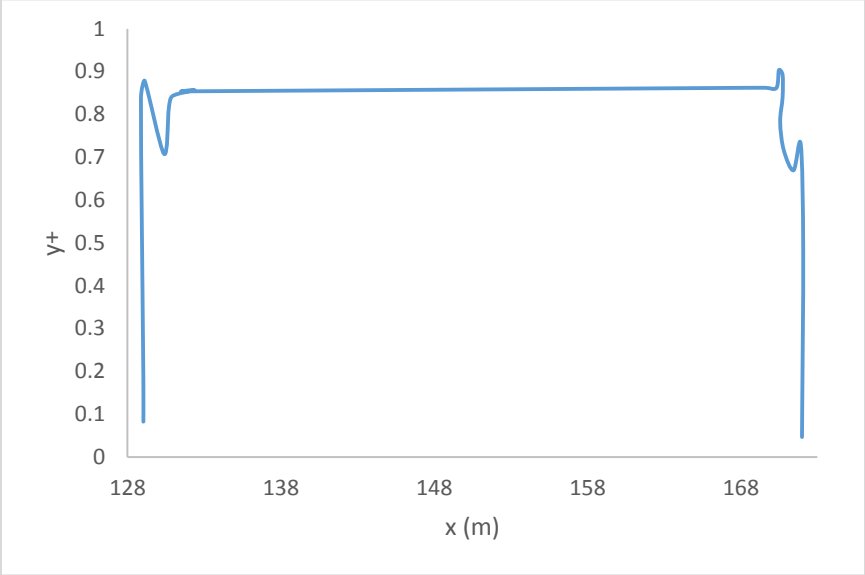

Figure 3: Distribution of the y+ value along the pod and tube wall at a pod speed of 400 m/s.

3.4.1. Coordinate System:

A number of coordinate systems could be selected for the numerical simulation. The coordinate systems that can be used are the absolute coordinate system, pod fixed coordinate system, and the shock fixed coordinate system. For the absolute coordinate system, all the parameters are defined for the global coordinates and the flow parameters are indicated without any subscript. Whereas, in the second coordinate system (i.e., pod fixed coordinate system), the

pods are assumed to be stationary while the flow is moving relative to the pods. Similarly, for the third coordinate system (i.e., the shock fixed coordinate system), the flow moves relative to the shockwave while the shock wave is assumed to be stationary. To differentiate the flow parameters represented in the different coordinate systems the subscript p and s are used for the pressure and Mach number values for pod fixed and shock fixed coordinate systems, respectively.

Research studies show that a compression wave is generated in front of the pod for the evacuated tube maglev train (ETMT)[13, 25, 29]. Due to the characteristics of the compression wave, the posterior compression wave has a faster speed than the preceding compression wave. This results in the accumulation of the compression waves at the head of the pods and hence it results in the formation of the high energy, non-linear shock waves. Moreover, the shock wave generated at the head of the pods travels in a direction normal to the direction of flow[16]. The normal shock wave moves faster as compared to the pod i.e. it appears to be leading the pod inside the tube, hence, it is given the name of the leading shock wave in this study[6, 16].

3.4.2. Converging-Diverging Nozzle Relation:

The flow in the case of the Hyperloop system encounters the variation of the area. The flow around the pods encounters the convergent section, the throat, and the divergent section. Thus, the converging-diverging relationships apply to the fluid flow around the pods of the Hyperloop System. The equation (1) provides the relationship between the change in the area to the Mach number and it is known by the name of the Area-Mach number relation[51].

$$\left(\frac{A}{A_{throat}}\right)^2 = \frac{1}{M^2}\left[\frac{2}{\gamma+1}\left(1+\frac{\gamma-11}{2}M^2\right)\right]^{\gamma+1/\gamma-1} \tag{18}$$

Where A and A_{throat} corresponds to the local cross-sectional area and the cross-sectional area of the throat inside the tube.

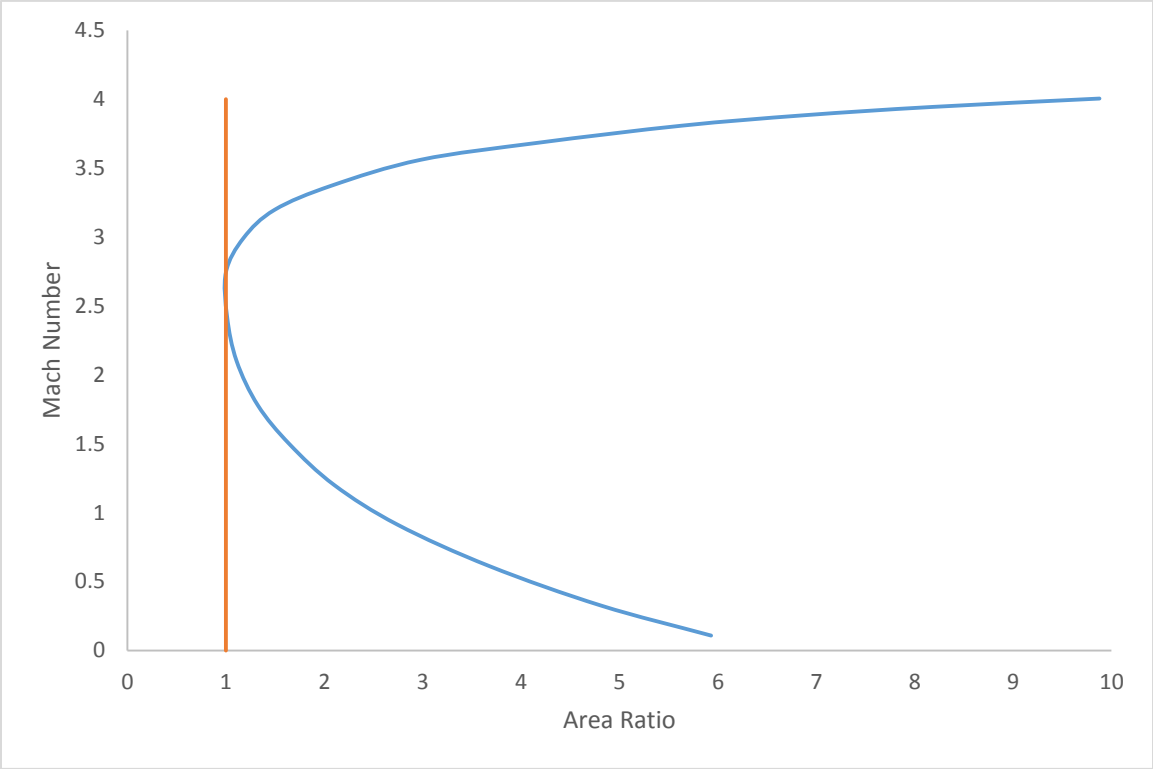

Figure 4: Area Mach Number Relation

The velocity of the fluid inside the convergent section of the pods exhibits the same behaviour as that of the flow in the case of the convergent section of the nozzle. However, in the case of the Hyperloop System, the pods are moving instead of the fluid around them. The variation of the Mach number with the area ratio is shown in figure 2. There is only one isentropic solution for supersonic flow. For the convergent section, the subsonic flow is accelerated, with the subsonic value of M dictated by the local value of $\frac{A}{A_{throat}}$. For the case when

$A = A_{throat}$ at the throat, $M = 1$. In that case, the flow in the divergent section expands supersonically[51], as seen in figure 2. Thus, like a converging-diverging nozzle, a similar kind of flow field behaviour is assumed for the Hyperloop System.

3.5. Verification:

3.5.1. Mesh Independence Test:

For the mesh independence test, the mesh size was set to be 0.1 m with coarse (135,474), medium (199,228), and fine (265,638) types. The mesh independence test was carried out for the pod speed of 300 m/s as it is close to the transonic regime along with the distance between the pods to be 3L. Additionally, the development of the shock wave (i.e., LSW and OSW) takes place at the transonic value, which affects the aerodynamic characteristics of the Hyperloop System. The distribution of the pressure value for coarse, medium, and fine mesh is shown in the figure. The percentage variation for the maximum pressure value is found to be 0.102 % and 0.456 %, respectively. Similarly, the variation of the aerodynamic drag value at the head of pods shows a difference of 0.1% and 0.15%, respectively. Based on this, the mesh size of 0.1 m with fine grid settings is applied to all the simulations for sufficient accuracy of the results.

3.5.2. Time Independence Test:

Three different time independence tests were conducted to find the sufficient value of the time step for the sufficient accuracy of the results. For the first case, the time step size was set to be 0.0005 s for the simulation time of 1s. So, the total number of time steps defined for this case

was 2000. For the second case, the time step size was set to be 0.001 s and hence the total number of time steps for this case were 1000. Similarly, for the third case, the time step size was set to be 0.005 s and the total number of time steps for this case was 200. A comparison of maximum pressure values for these analyses shows a percentage difference of 0.22 % and 0.95 % respectively. Additionally, a comparison of drag force acting on the first and second pod shows a difference of 0.307 % and 1.046 % for the first pod and 0.937 % and 0.078 % for the second pod, respectively for these three cases. Based on this, the time step size for the second case was selected to get sufficiently accurate results.

Chapter No. 4

This chapter deals with the numerical results of the designed model. The parameters that are evaluated for the aerodynamic analysis of the Hyperloop System are the speed of the pods, the distance between the pods, the pressure distribution around the pods and temperature distribution. All these results are described in detail in this chapter.

4. Results & Discussion:

In this research, the results of the multi-pod Hyperloop system under the compressible flow conditions are studied in terms of the reference frame moving at the same speed as that of the walls of the pod. The distance between the pods of the Hyperloop system is a crucial factor, related to the pressure and Mach number distribution inside the tube tunnel. The optimal distance between the pods should be maintained so that the interaction between different kinds of shockwaves (i.e. normal and oblique) and shockwave boundary layer interaction could be avoided, as it affects the flow regime around the second pod and hence severely affects its performance[52]. The results of the simulation were retrieved for a simulation time of 1s.

4.1. Flow Distribution:

The flow through the single pod Hyperloop system is like the converging-diverging nozzles. This is because the flow in the Hyperloop system encounters a similar change in the cross-sectional area as like a converging diverging nozzle. But the main difference between the flow in the Hyperloop system and that of the converging-diverging nozzle is that the pods are moving inside the tube while the fluid (air) is stationary, whereas, in the case of the converging-diverging nozzle the fluid moves through the channel. The motion of the pods inside the tube results in compression of the fluid i.e., air at the frontal area or the nose of the pods. This compression of the air particles results in the formation of a compression wave (i.e., normal shock wave) without the chocking of the fluid at the throat section of the tube. Based on the speed of the pods inside the tube, the flow regime can be divided into three different categories[16]. For the Multi-pod Hyperloop System, the distribution of the Mach number for each category is shown in Figure 3.

If the flow speed (i.e., Mach Number) at the inlet of the convergent section of the tube is lower as compared to the critical value of the flow speed (i.e., $Ma_{critical}$). The flow will not be accelerated to the sonic speed at the throat section of the tube. This results in the deceleration of the flow in the divergent section of the tube and hence the flow will remain subsonic at the tail section of the first pods[16], as seen in Figure 3. A similar phenomenon is true for the second pod as well, as seen in Figure 4.

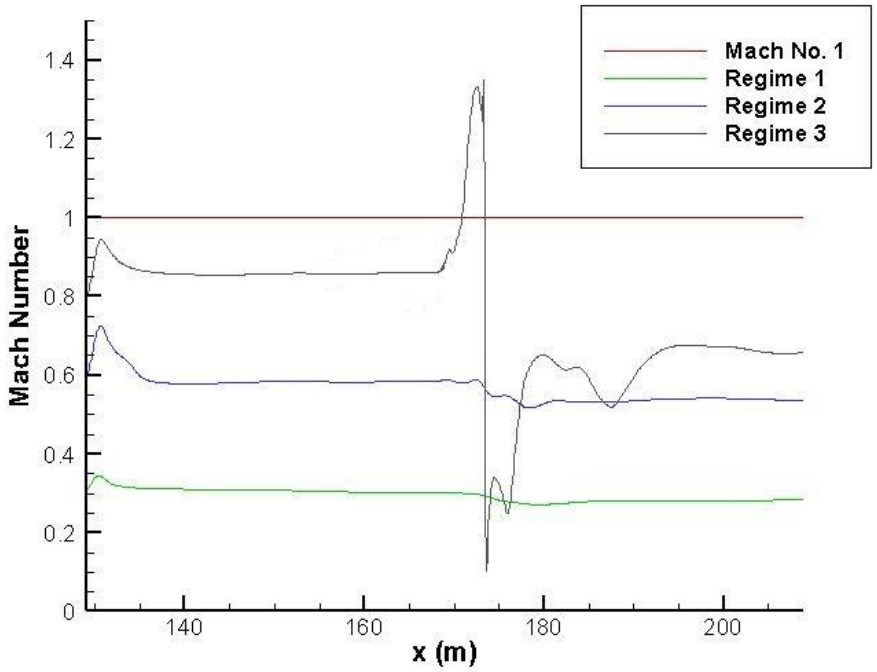

Figure 5: Flow Regime around the first pod

Now if the speed of the flow is equivalent to the critical value of the Mach number, the flow will be accelerated through the convergent section of the tube and the flow speed will be sonic at the throat section of the pods. This will result in acceleration of the flow to the supersonic speed in the divergent section of the tube. But due to the interaction of two opposite flows i.e., from the tail of the first pod (trailing flow) and the head of the second pod (leading

flow), the flow at the tail section is disturbed due to the change in the pressure-flow filed. Hence, the flow at the tail of the first pod does not accelerate to the appropriate, as seen in Figure 3. However, the boundary layer separation phenomenon will be observed at the tail of the second pod. This will result in the formation of the oblique shockwave at the tail section of the second pods. Moreover, due to the existence of the oblique shock wave, the flow does not accelerate to the supersonic speed, which results in the deceleration of the flow through the divergent section of the tube[16] for the second pod. If the speed of the pods is increased further, the oblique shockwave is pushed to the end of the divergent section of the tube for the second pod. This results in the acceleration of the flow through the divergent section of the second pod, which results in higher Mach number flow, as seen in Figure 3. Additionally, an oblique shock wave starts to appear for the first pod due to the increase in the strength of the flow. But due to its interaction with the leading shock wave from the first pod, it disappears immediately after its interaction, as seen in Figure 4.

The oblique shockwave gets swept out of the divergent portion of the second pod if the speed is increased further. Thus, with the increase in speed value of the pods, the flow is accelerated to the top limit of the Mach number for the given divergence area ratio, while the Mach number of the flow behind the second pod stays unchanged[16], as seen from Figure 3.

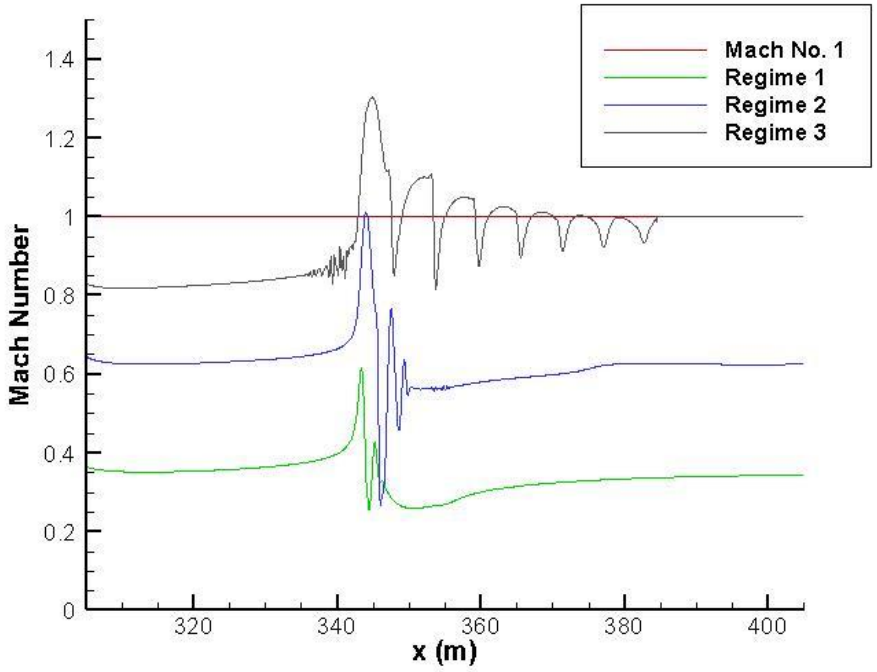

Figure 6: Flow Regime around the second pod

4.2. Distance Between the Pods:

The distance between the pods of the Hyperloop system is a key factor, as this distance affects the aerodynamic characteristics of the second pod. So, there should be an optimal distance between the two pods, as the interaction of the oblique shockwave generated at the tail of the first pod and the normal shockwave generated at the tip of the second pod causes a disturbance in the flow regime around the pods and hence, affects the aerodynamic characteristics of the pods.

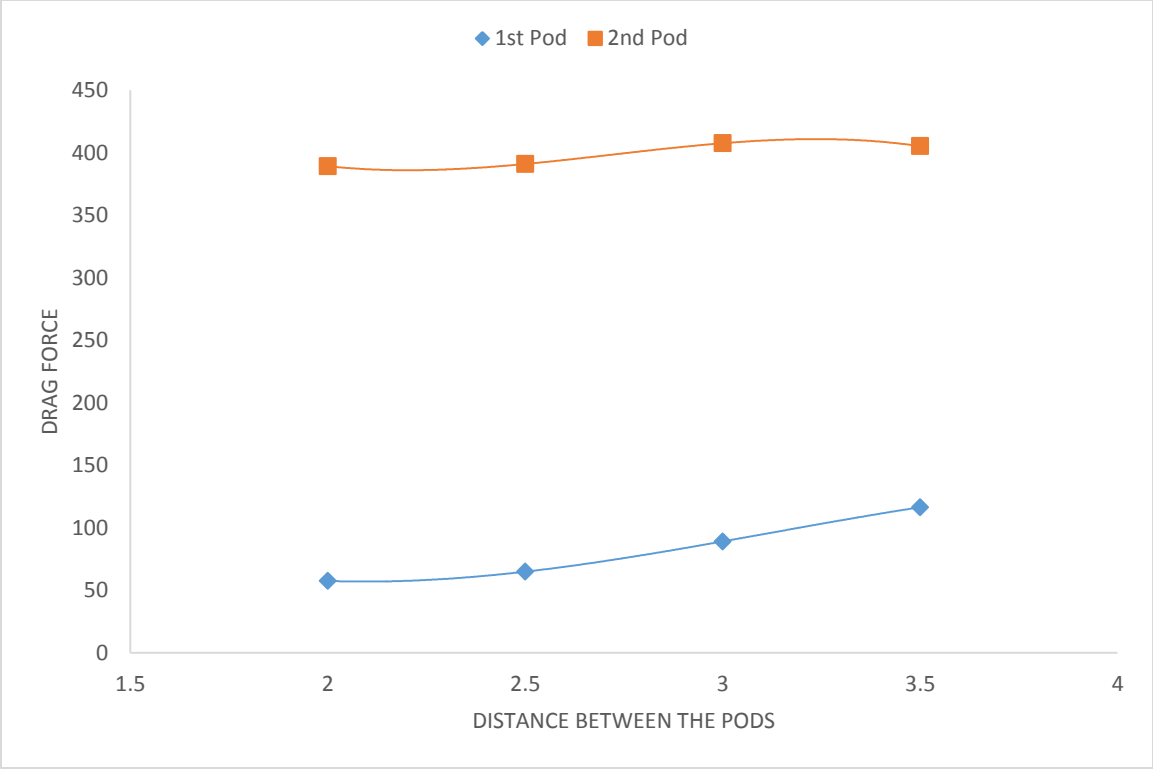

Figure 7: Total Drag force variation with the increase in distance between the pods at the speed value of 100 m/s

Normal and oblique shockwaves, both are destructive, and their interaction is a more destructive phenomenon, especially when the two waves are moving in the opposite direction and this interaction should be avoided at any cost. Although there are no other systems in which two opposing shockwaves interact with each other, in the case of the Hyperloop system, for the movement of multiple high-speed pods through lower pressure tub, the interaction becomes a crucial factor.

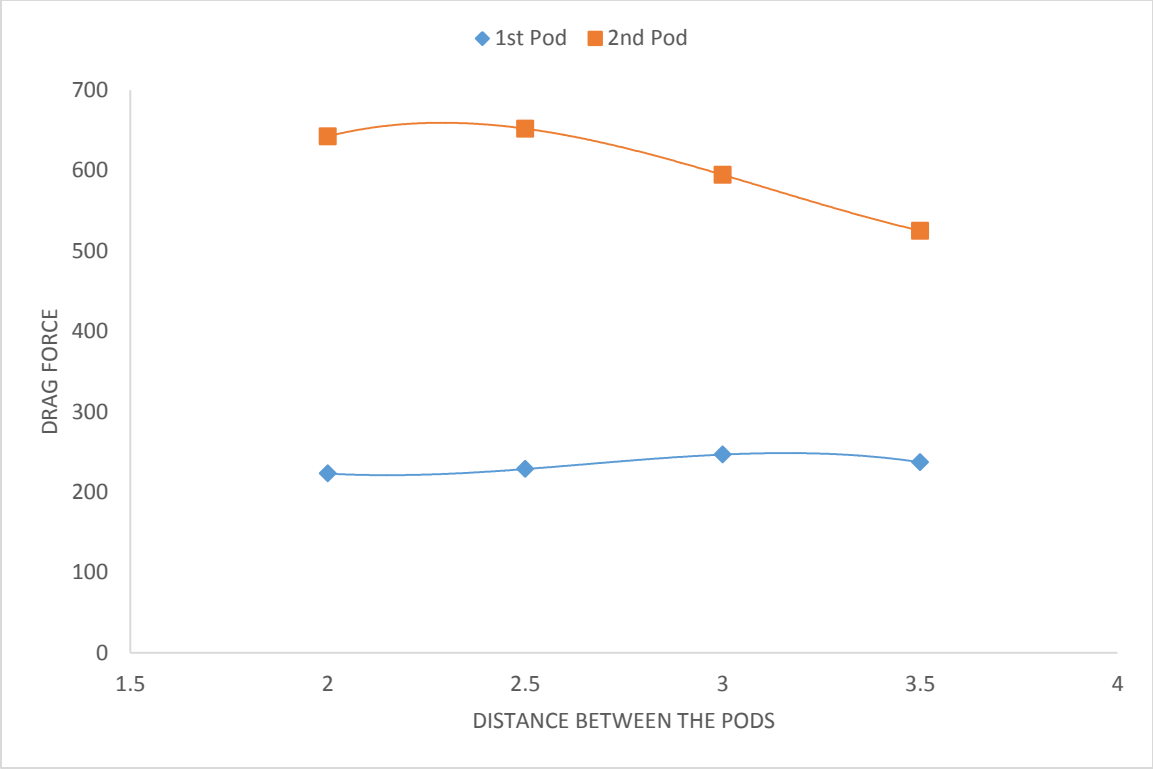

Figure 8: Total Drag force variation with the increase in distance between the pods at the speed value of 200 m/s

When the distance between the two pods is in the range of 2L to 2.5L, a pressure fluctuation is observed in the frontal region of the second pod i.e., at the entrance of the convergent section of the second pod. This pressure fluctuation is due to the interaction of the oblique shockwave at the divergent section of the first pod and the normal shockwave at the convergent section of the second pod. This pressure fluctuation results, in inconsistent pressure distribution in the flow regime of the second pod. A dip in pressure value is observed for a brief period, afterwards with a consistent rise in pressure, just before the throat of the second pod, as seen from Figures. Due to this inconsistent rise in pressure value, a disturbance in the drag is observed for the second pod.

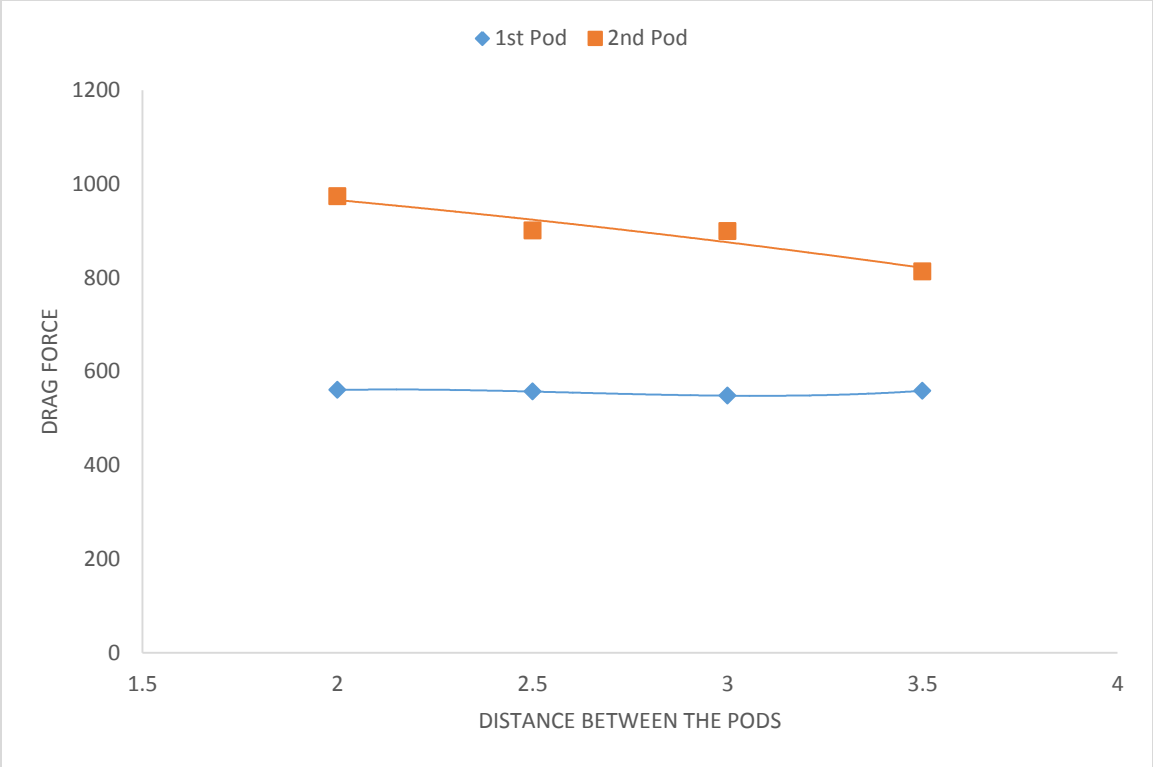

Figure 9: Total Drag force variation with the increase in distance between the pods at the speed value of 300 m/s

It is also observed that for the pod's speed of 400 m/s, the drag force value on the first pod increases with the increase in the distance between the pods, this is due to the interaction of the particles in between the pods, a large pressure gradient is developed around the first pod and which results into the large value of the drag. When the distance between the pods is small, the pressure gradient due to the interaction of the trailing oblique shock wave at the tail section of the first pod and the leading shock wave at the throat section of the first pod is also small, this results in lower value of drag around the first pod. But when the distance between the pods increases, the pressure gradient around the first pod also increases due to the interaction of the lower pressure value obtained by the trailing oblique shock wave and the high-pressure value of the leading shock wave. This results in an overall smaller rise in the pressure value between the two pods and hence a large pressure gradient around the first pod. This results in an increase in the drag force around the first pod.

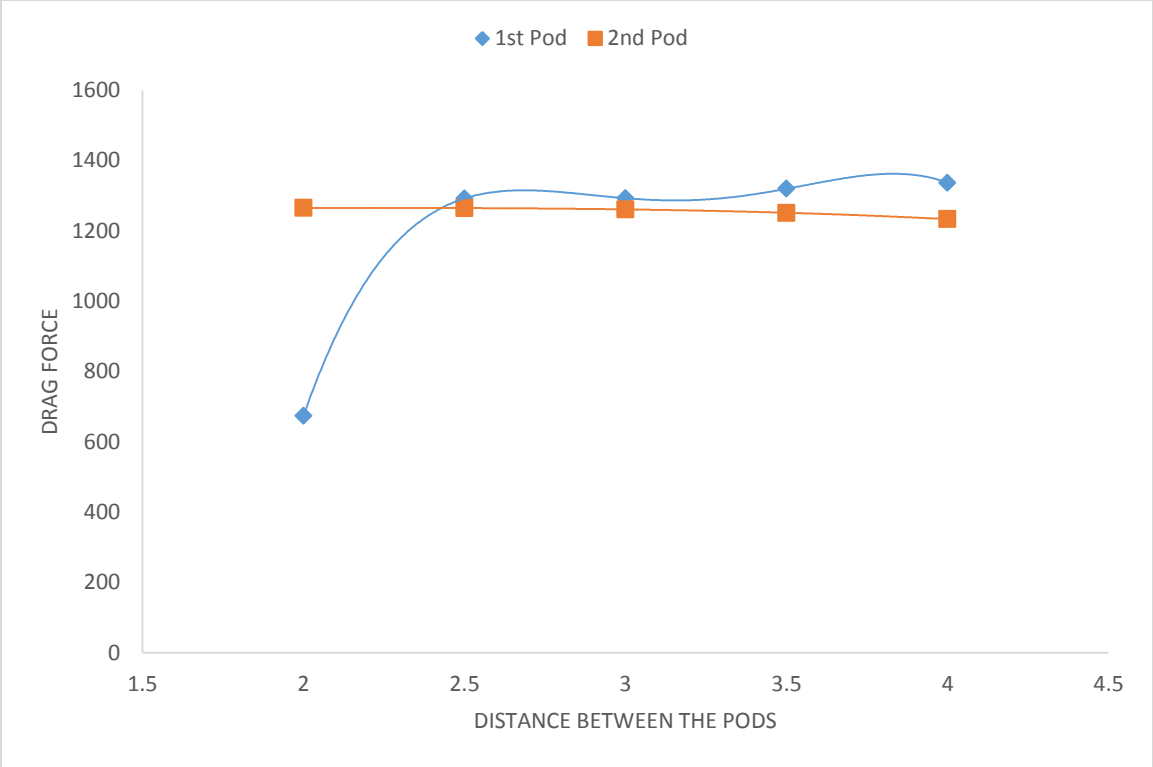

Figure 10: Total Drag force variation with the increase in distance between the pods at the speed value of 400 m/s

Whereas a different kind of behavior is observed for the second pod. The drag force decreases with the increase in the distance between the pods. This is due to the lower pressure gradient value around the second pod i.e., the normal shock wave interacts with the oblique shock wave. The trailing oblique shock wave results in a large decrease in the pressure value, whereas a leading normal shock wave results in an exceptionally substantial increase in the pressure value. Moreover, the lowest pressure value for the trailing oblique shock wave exists at the end region i.e., where the oblique shock wave is about to end.

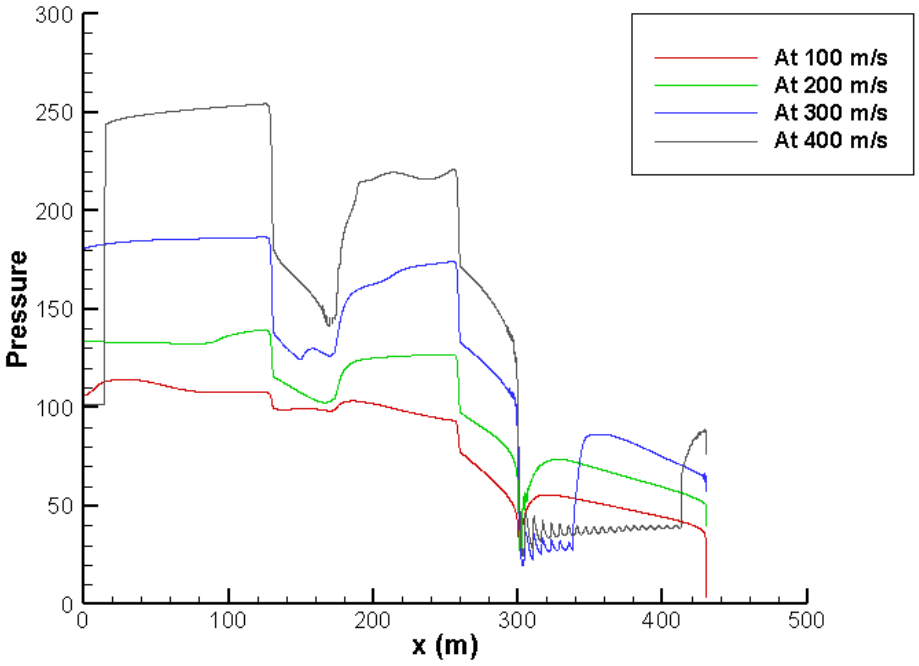

Figure 11: Pressure Distribution long the tube at the pod distance of 2L

Similarly, when the distance between the pods is small i.e., 2L to 3L, the pressure decrease in the oblique shock wave is also small. When it interacts with the normal shock wave, it results in a larger rise in the pressure value in between the pod. This large rise in the pressure value results in a larger value of drag force on the second pod. But, when the distance between the pods is increased to a large value i.e., 3.5Lto 4L, the normal shock wave interacts with the diminishing oblique shock wave. This results in a lower pressure value in the frontal section of the second pod, and hence a lower drag value.

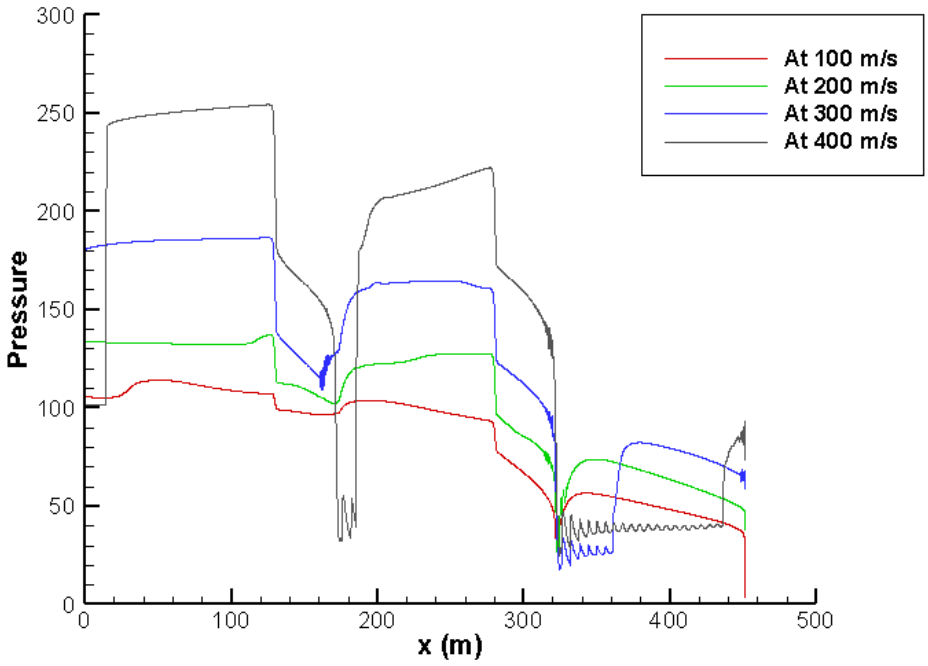

Figure 12: Pressure Distribution long the tube at the pod distance of 2.5L.

Hence, increasing the distance between the pods help to eradicate this pressure disturbance in front of the second pod (i.e., in the convergent section of the second pod). When the distance between the pods is increased to 3.5L, the pressure distribution in front of the second pod becomes smooth and hence, a consistent value of drag force is observed for the second pod, as seen from the **figure**.

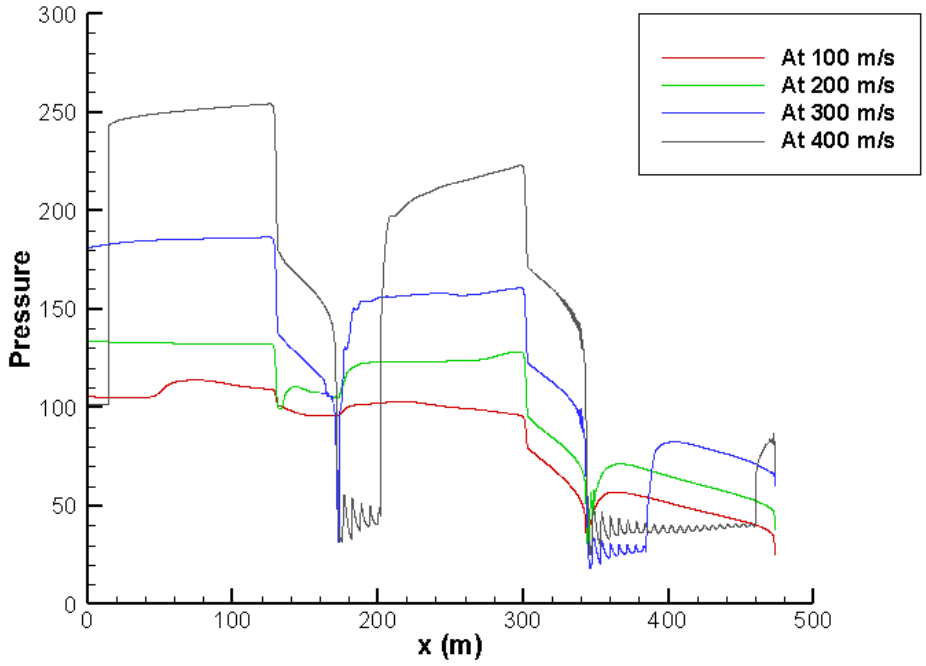

Figure 13: Pressure Distribution long the tube at the pod distance of 3L.

4.3. Pressure Waves:

Several pressure waves and shockwave boundary layer interactions occur in the flow regime. A shockwave is produced under supersonic conditions, but in the case of an Hyperloop system, a compression wave propagates through the frontal area of the pod. As the pod travels through the tube, the air particles accumulate at the head of the pods and are dispersed downstream of the pods. The accumulation of the air particles results in the development of the high-pressure region, whereas the dispersion of the air particles behind the pods results in lower pressure regions. Moreover, a compression wave is generated at the head of the pods and an expansion wave is generated at the tail of the pods. These compression waves travel in the direction of motion of the pod, while the expansion wave propagates opposite to the direction of motion of the pods.

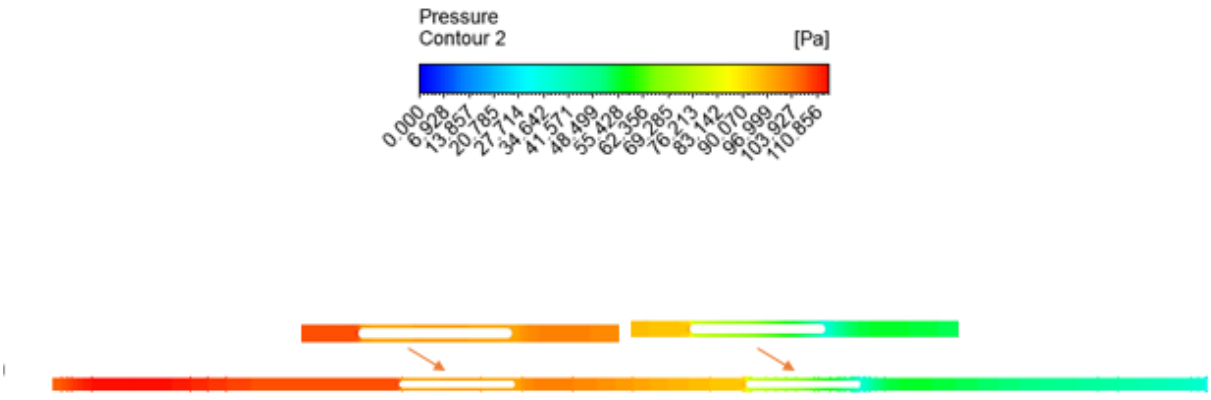

Figure 14: Pressure Distribution around the pods for 100 m/s speed value at the distance of 2L between the pods

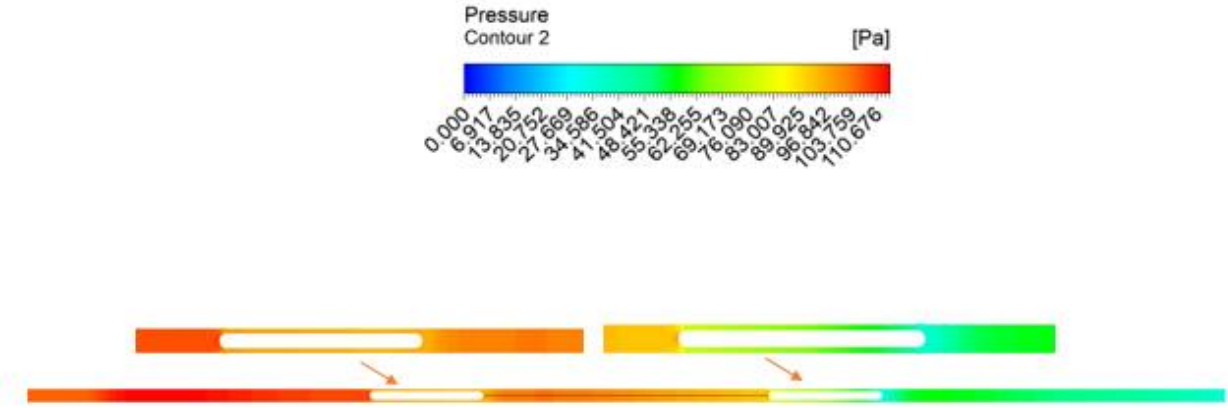

Figure 15: Pressure Distribution around the pods for 100 m/s speed value at the distance of 2.5L between the pods

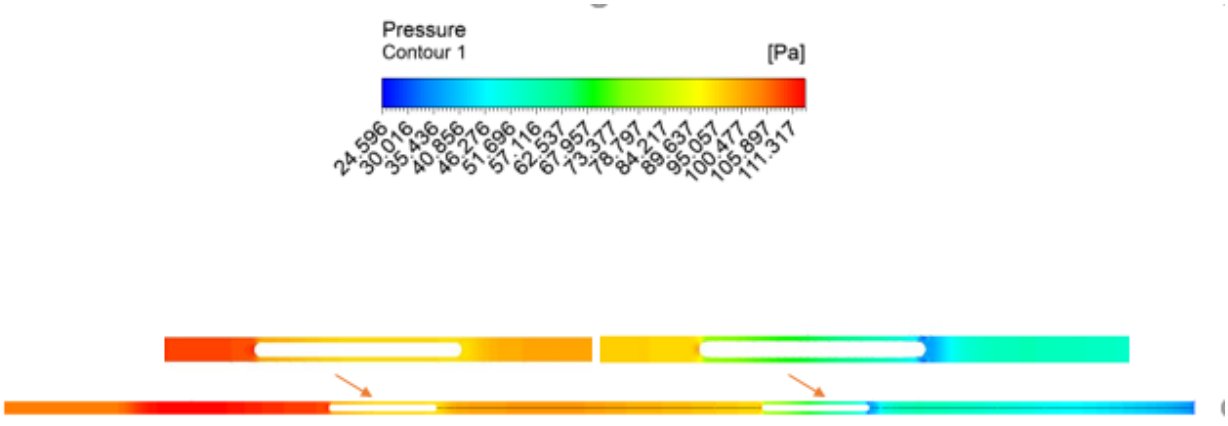

Figure 16: Pressure Distribution around the pods for 100 m/s speed value at the distance of 3L between the pods

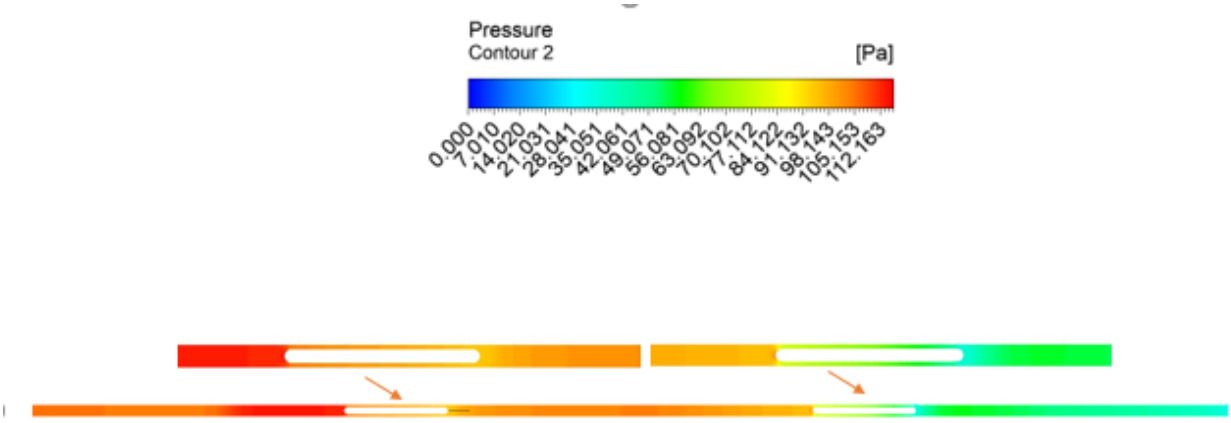

Figure 17: Pressure Distribution around the pods for 100 m/s speed value at the distance of 3.5L between the pods

Because of the characteristics of the compression wave, the posterior compression wave moves faster than the precedent compression wave. This results into the compression of the compression waves, which results into the formation of the normal shock wave, which is non-linear in nature. The forward pressure waves, as seen in Figures 11-14, 15-18, 19-22, and 23-26 evolve into the leading shock wave (LSW) for all flow regimes. Moreover, the formation of oblique shock wave (OSW) is observed at high pod speed close to the tail section of the pods. The expansion wave, on the other hand, is dispersed throughout its propagation and does not evolve into the conventional shock wave[16].

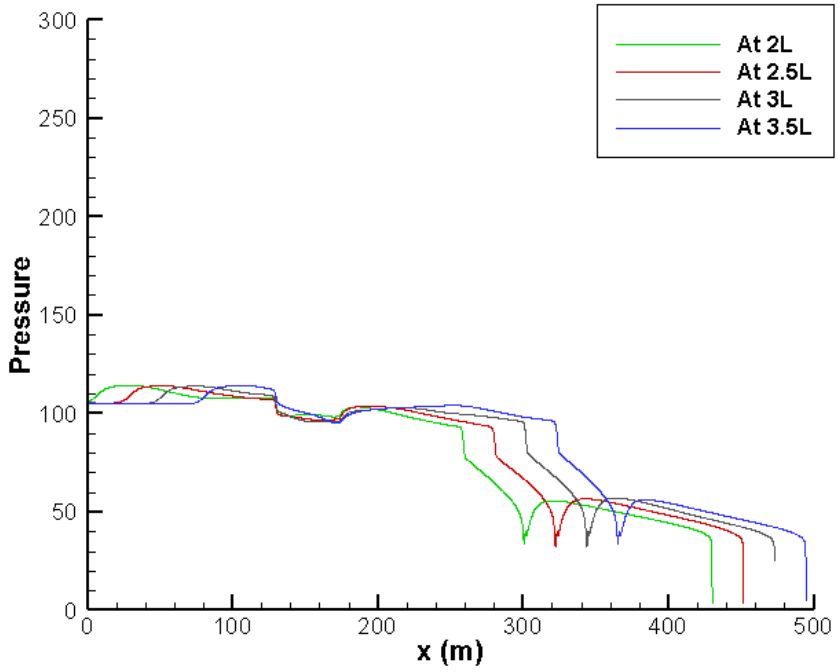

Figure 18: Pressure Plots at 100 m/s

The generation of the compression waves results in a significant rise in the pressure value at the frontal section of the pods. Especially for the case of the first pod, which experiences a normal shock wave-like phenomenon due to a significant rise in the pressure value. The pressure increases till the throat section of the first pod and then starts to decrease. The pressure reaches a minimum value at the throat section of the first pod. When the distance between the two pods is small (i.e., 2L to 2.5L) this pressure value starts to increase again due to the existence of the second pod behind it, as seen in Figure 11. Moreover, the second pod experiences a large pressure value like the first pod, but this pressure value is relatively small as compared to the pressure at the head section of the first pod, as seen in Figure 47. The relatively lower value of pressure is due to the interaction of the low-pressure wave generated at the tail section of the first

pod and the high-pressure wave generated at the head section of the second pod. The pressure value then increases in the same way till the throat section of the second pod and finally starts to decrease along the length of the divergent section of the second pod.

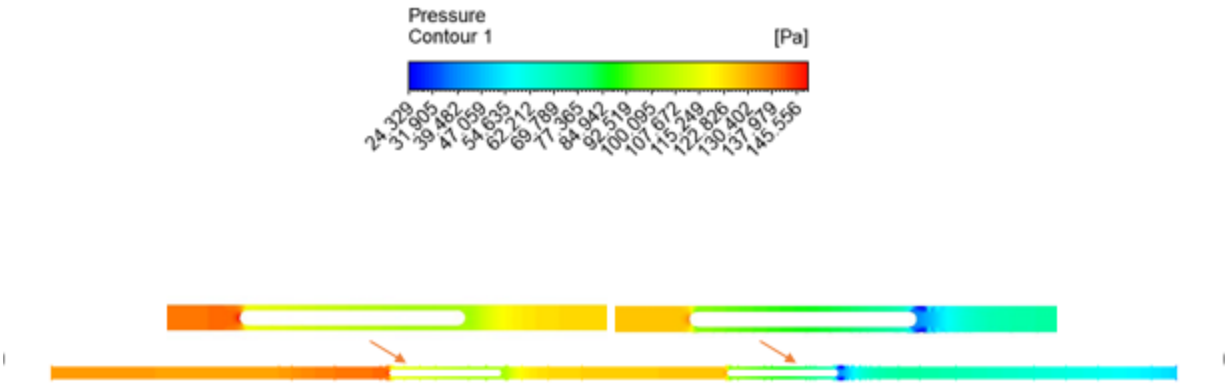

Figure 19: Pressure Distribution around the pods for 200 m/s speed value at the distance of 2L between the pods

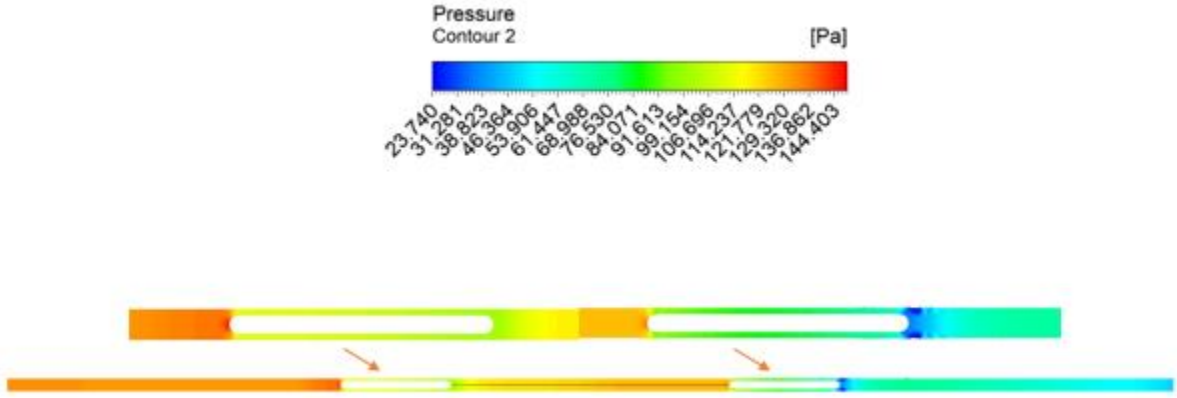

Figure 20: Pressure Distribution around the pods for 200 m/s speed value at the distance of 2.5L between the pods

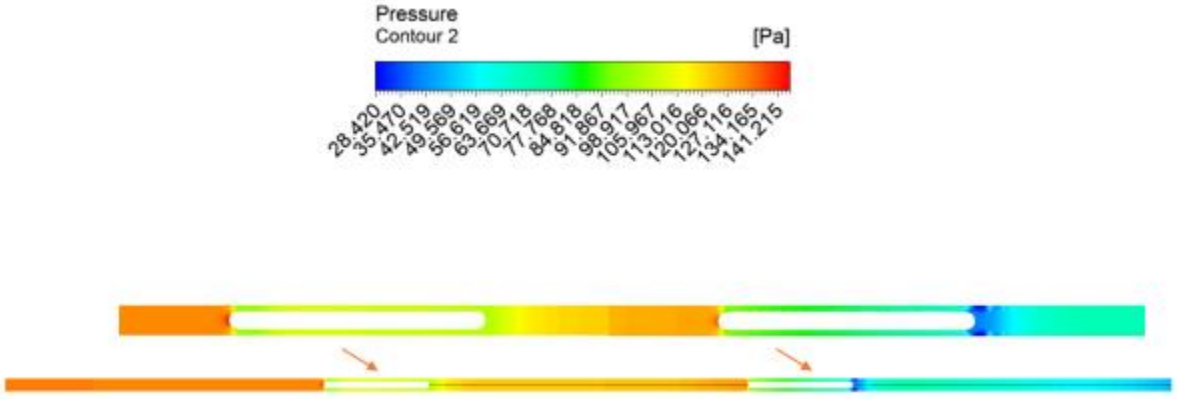

Figure 21: Pressure Distribution around the pods for 200 m/s speed value at the distance of 3L between the pods

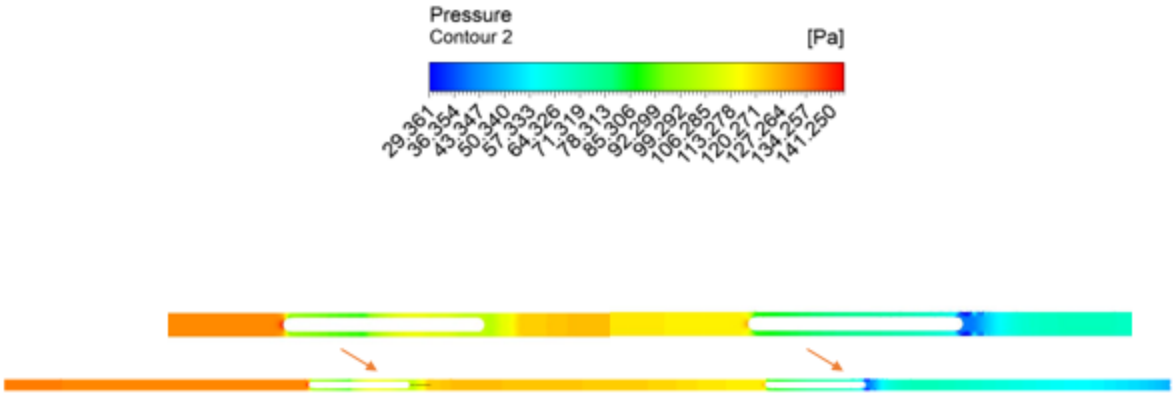

Figure 22: Pressure Distribution around the pods for 200 m/s speed value at the distance of 3.5L between the pods

Increasing the distance between the two pods delays the interaction of the two pressure waves, as seen in Figures 12-14. Increasing the distance between the two pods results in the shifting of the pressure wave interactions in the space between the two pods. Initially, when the distance between the pods was 2L, the pressure wave interaction was taking place close to the throat or at the entrance of the divergent section of the first pod. But when the distance between the pods is increased (i.e., at 3.5L) the interaction of the pressure waves takes place in space between the two pods i.e., at the end of the divergent section of the first pod and close to the entrance of the convergent section of the first pod, as seen in Figure 14. This results in a decrease in the pressure value in the divergent section of the first pod and a relatively higher value of pressure in the convergent section of the second pod, as seen in Figure 47. Moreover, the total drag force starts to increase on the first pod with the increase in the distance between the pods and decreases on the second pod, as seen in the above figure.

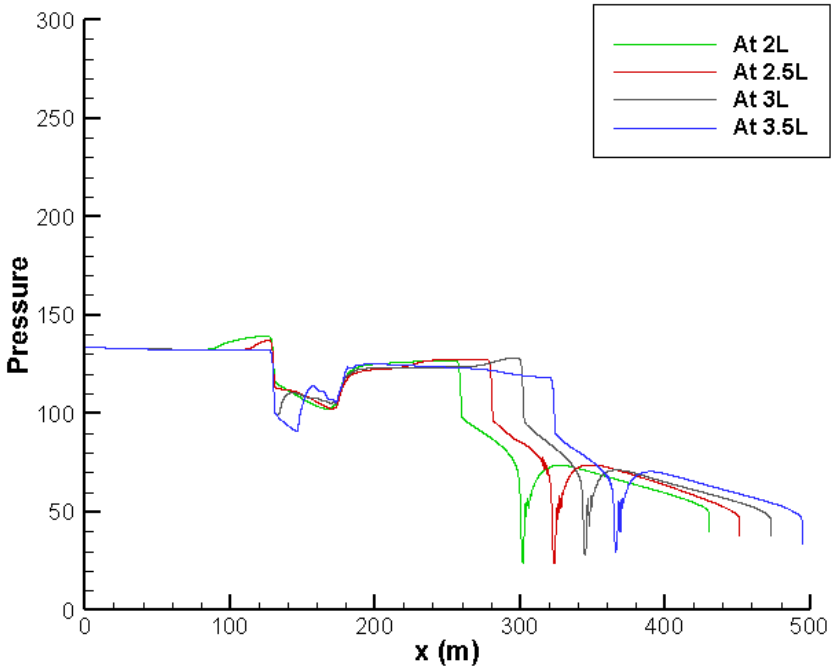

Figure 23: Pressure Plots at 200 m/s

No oblique shock wave is observed at the divergent section of the first pod at a lower distance value between the pods (i.e., 2L to 3.5L) in flow regime 2. This is because, the flow is not sufficiently accelerated through the convergent section of the first pod, due to the small pressure gradient between the head and tail of the first pod. The leading shock wave from the second pod reaches the throat of the first pod rapidly due to the small distance between the two pods, to preserve the conditions for conservations of mass, the velocity in between the gap between the two pods decreases i.e., which results in a low value of Mach number (i.e., high-pressure value) at the tail of the first pod as compared to the critical value of Mach number sufficient to allow the formation of the oblique shock wave. However, a pressure fluctuation region is formed along the length of the first pod, as seen in Figure 15-18. Increasing the distance between the pods results in the formation of the oblique shock wave at the divergent section of

the second pod, because the flow is sonic at the throat section of the second pod in flow regime 2.

Additionally, an oblique shock wave also appears in the divergent section for the second pod, because the flow is sonic at the throat section of the second pod in flow regime 2. This is due to the relative motion, the annular shape gab, and the viscosity effects between the pod and tube wall leading to the normal shock wave to be inclined on the wall and as a result preserving the wall boundary condition as a result an oblique shock wave is generated due to this reflection of the shock wave form the tube wall boundary. In regime 2, the position of the oblique shock wave is set at the point where the propagation speed of the oblique shock wave and the flow speed are balanced, independent of flow time, as illustrated in Figures 15-18.

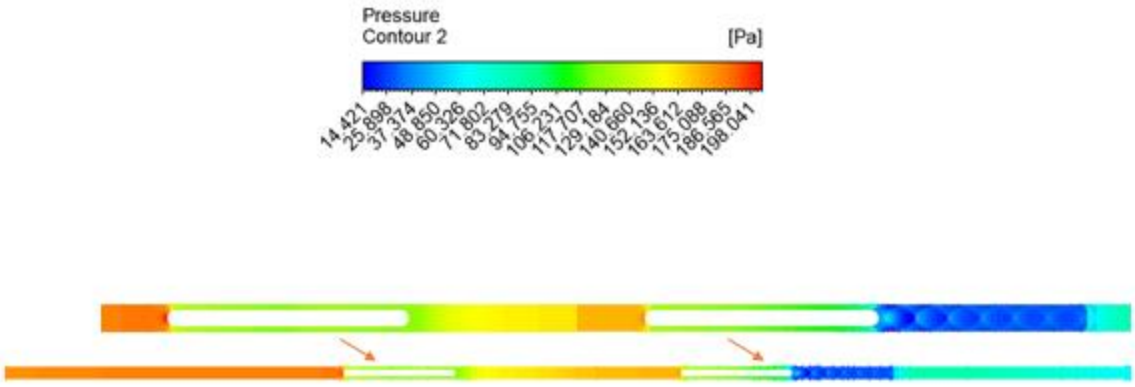

Figure 24: Pressure Distribution around the pods for 300 m/s speed value at the distance of 2L between the pods

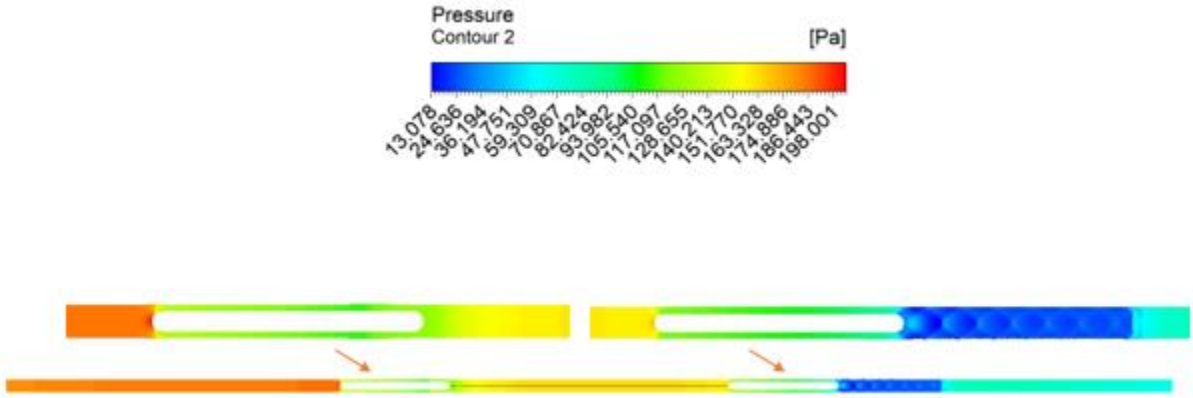

Figure 25: Pressure Distribution around the pods for 300 m/s speed value at the distance of 2.5L between the pods

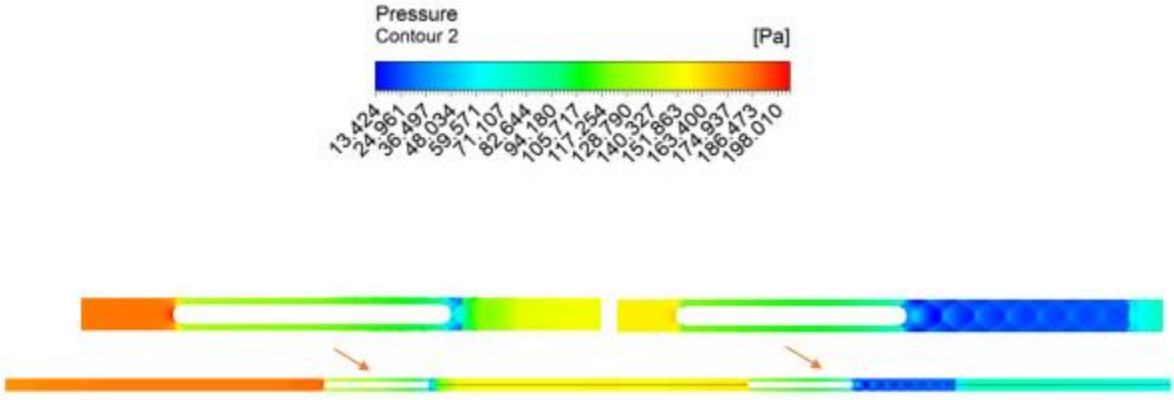

Figure 26: Pressure Distribution around the pods for 300 m/s speed value at the distance of 3L between the pods

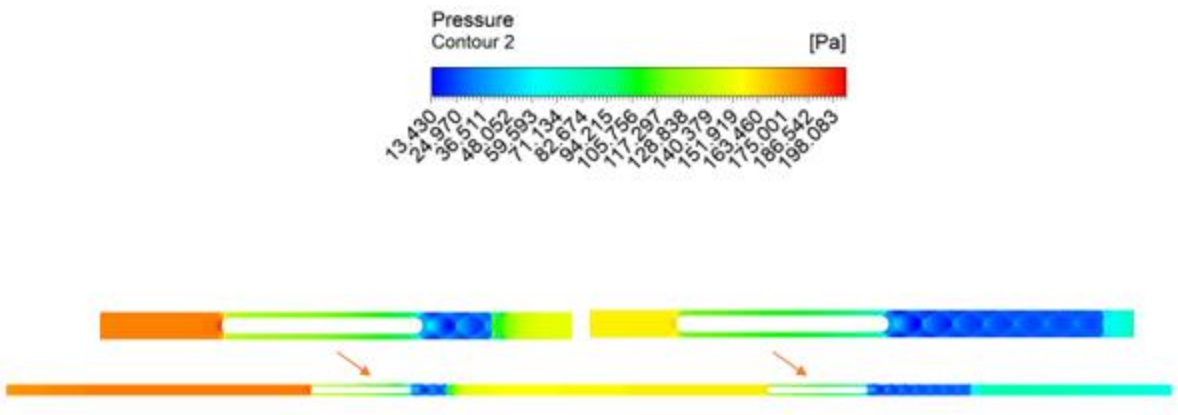

Figure 27: Pressure Distribution around the pods for 300 m/s speed value at the distance of 3.5L between the pods

In the flow regime 3, increasing the pod speed exhibits a similar phenomenon, except for the fact that interaction of oblique shock wave and normal shock wave exists in between the two pods, which results in a maximum rise in the pressure value for the second pod. Finally, an oblique shock wave exists at the tail section of the second pod at a larger speed value i.e., at 300 m/s and 400 m/s, as seen in Figures 19-22, and 23-26, followed by an expansion region at the end of the tube. There is a rapid rise in pressure due to the leading shockwave, and the pressure value decreases behind the leading shockwave. A similar kind of pressure distribution is observed in the case of high-speed train tunnels. Before the forward expansion wave passes through the pod, the flow accelerates to sonic speed, particularly at speeds of 300 and 400 m/s.

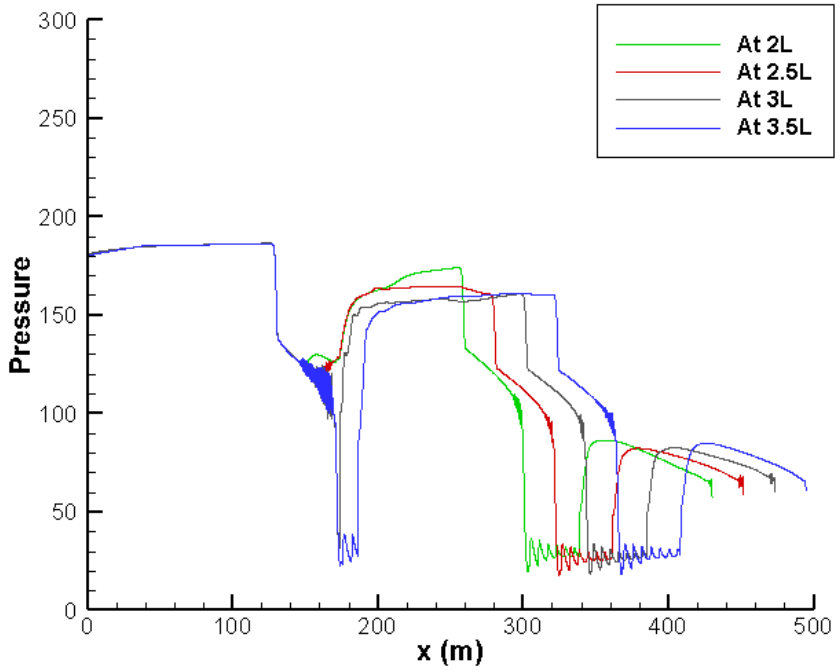

Figure 28: Pressure Plots at 300 m/s

As seen in Figures 19-22, and 23-26, in this situation, no interaction zone is produced upstream of the first pod since the forward expansion wave is unable to propagate across the first pod. A different kind of behaviour is observed for the second pod. Because there is an oblique shockwave in front of the second pod due to the existence of the first pod, there is a decrease in pressure in the frontal region of the second pod. But due to the normal shockwave generated by the compression of the air in front of the second pod, a large pressure exists at the entrance to the convergent section of the second pod. The increase in pressure rise for the second pod is lower and is explained by the fact that an oblique shockwave exists in front of the second pod, which is responsible for a considerable decrease in pressure. However, this pressure rise is lower as compared to the pressure rise in the case of the first pod. Moreover, an interaction region is developed at the tail of the second pod due to the interaction of the receding shock wave and the backward expansion wave. Since the direction of propagation of the second pod and the receding

shock wave are the same, so it passes through the pod regardless of the pod speed. As a result, the downstream interaction zone can be observed in all flow regimes[16].

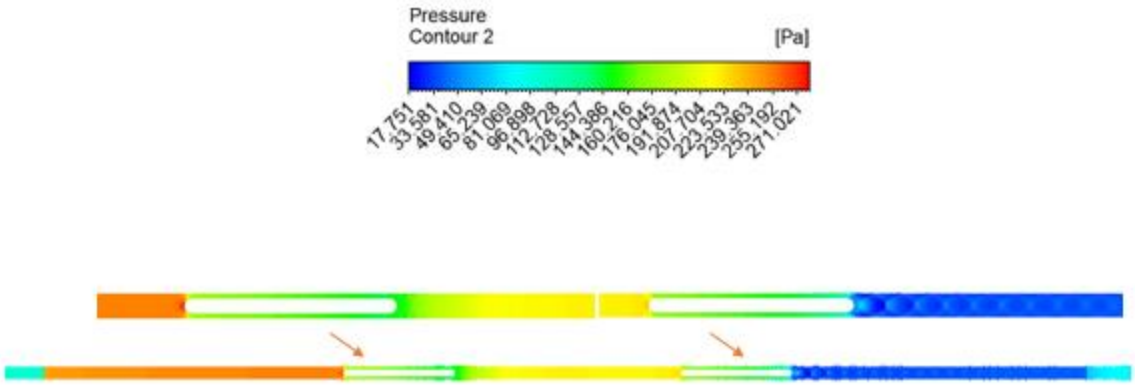

Figure 29: Pressure Distribution around the pods for 400 m/s speed value at the distance of 2L between the pods

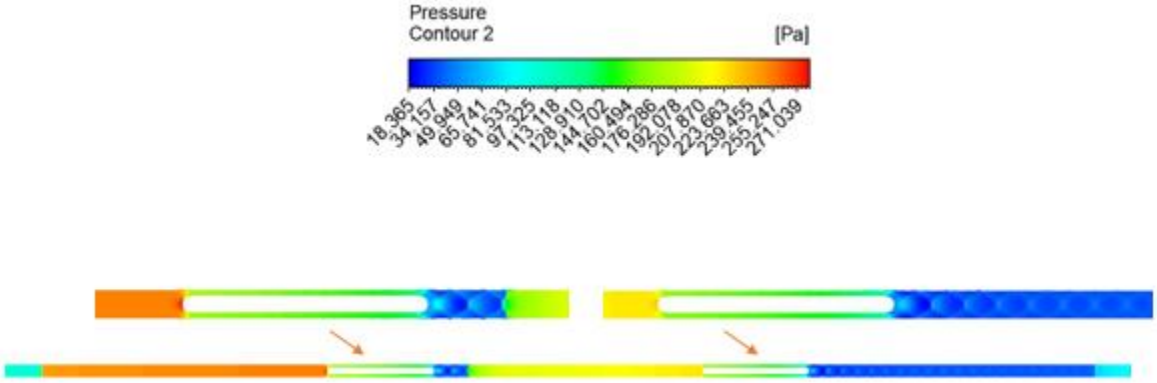

Figure 30: Pressure Distribution around the pods for 400 m/s speed value at the distance of 2.5L between the pods

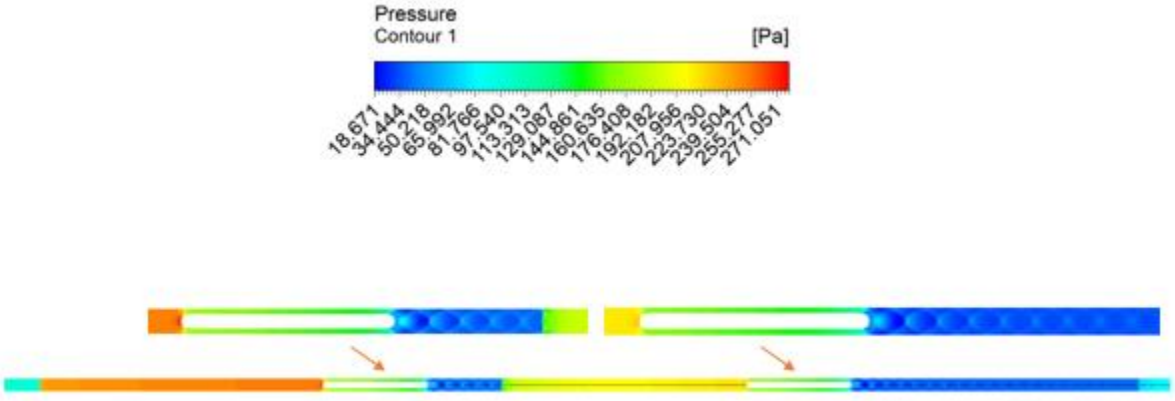

Figure 31: Pressure Distribution around the pods for 400 m/s speed value at the distance of 3L between the pods

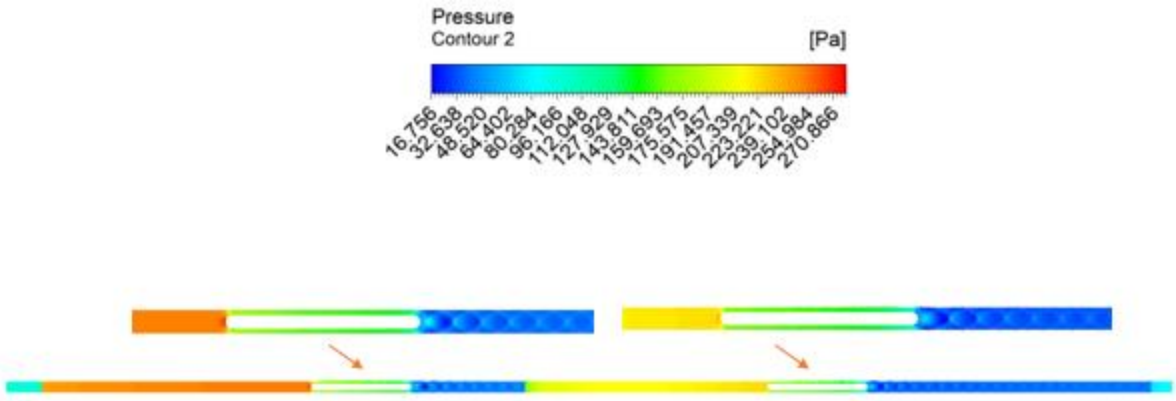

Figure 32: Pressure Distribution around the pods for 400 m/s speed value at the distance of 3.5L between the pods

Similarly, the oblique shock wave does not appear at the tail section of the first pod due to the smaller distance value between the pods (i.e., 2L to 2.5L). When the distance between the pods is increased to 3L and 2.5L for 300 m/s and 400 m/s pod speed, respectively, the oblique shock wave appears at the tail section of the first pod. However, for the second pod, when the flow is fully accelerated in regime 3, the oblique shock wave is swept downstream. As a result, the oblique shock wave extends downstream and the trailing shock wave propagates away from the pod at the end of the oblique shock wave, as seen in Figures 19-22, and 23-26.

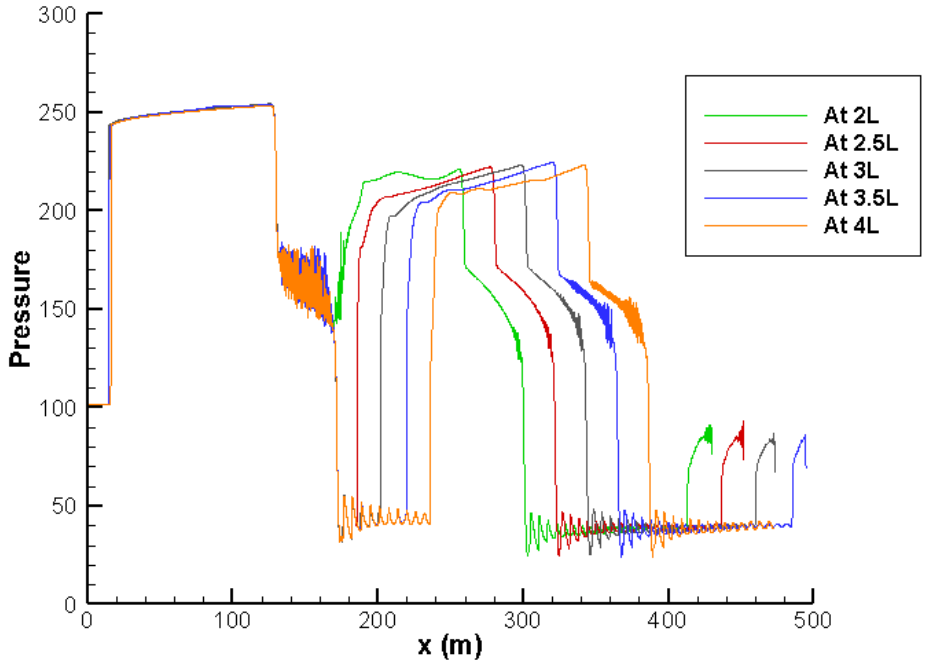

Figure 33: Pressure Plots at 400 m/s

4.4. Mach Number and Pressure Field Distribution:

Eq. (1) is used to get the subsonic solution i.e., 0.408 and supersonic solution 1.91 for the blockage ratio of 0.36. The subsonic solution is representing the M_{in}^{p} for the isentropic flow under the chocking condition and the supersonic solution represents the M_{ex}^{p} for the isentropic flow under the chocking conditions. The critical Mach number is represented by $M_{cr,isen}$. No sonic flow exists at the throat section of the pods in flow regime 1. Moreover, the pod's speed is 100 m/s corresponding to the flow regime 1. Due to the leading shock wave, the Mach number decreases for the frontal region of both pods of the multi-Pod system, and the value of Mach number found for the frontal region of the first pod is 0.35, as seen in Figure 38. This value of Mach number remains the same no matter what the distance between the pods is. However, the

Mach number found in the frontal section of the second pod is found to be greater than the critical value of the Mach number. The Mach number found in the frontal section of the second pod is 0.425. This is due to the deceleration of the flow field followed by a sudden acceleration at the frontal section of the second pod. This higher value of the Mach number causes the flow field to accelerate till the end of the throat section of the second pod. As a result, the Mach number increases followed by a sudden decrease in the throat section, as seen in Figure 38. Thus, although the first pod is travelling at a higher speed as compared to the critical Mach number $M_{cr,isen}$, the leading shock wave reduces the M_{in}^{p} below $M_{cr,isen}$ for the first pod and delaying the choking of the flow. But for the second pod, the effect of the leading shock wave at the frontal section of the pod is suppressed by its encounter with the expansion of the flow regime generated at the tail section of the first pod. This results in higher value of Mach number for the frontal section of the second pod. Moreover, with the increase in the distance between the pod, the Mach number is accelerated to higher values at the end of the throat section of the second pod, as seen from Figure 34-38.

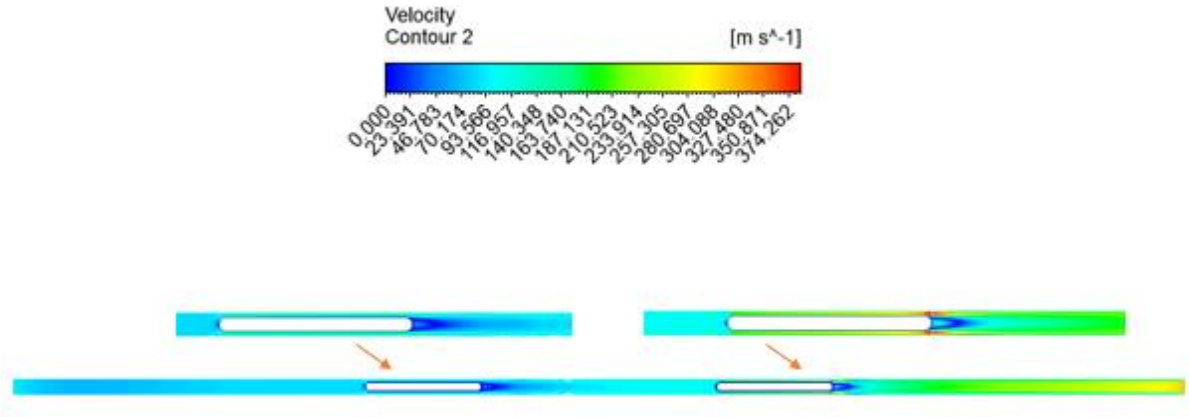

Figure 34: Velocity Distribution around the pods for 100 m/s speed value at the distance of 2L between the pods

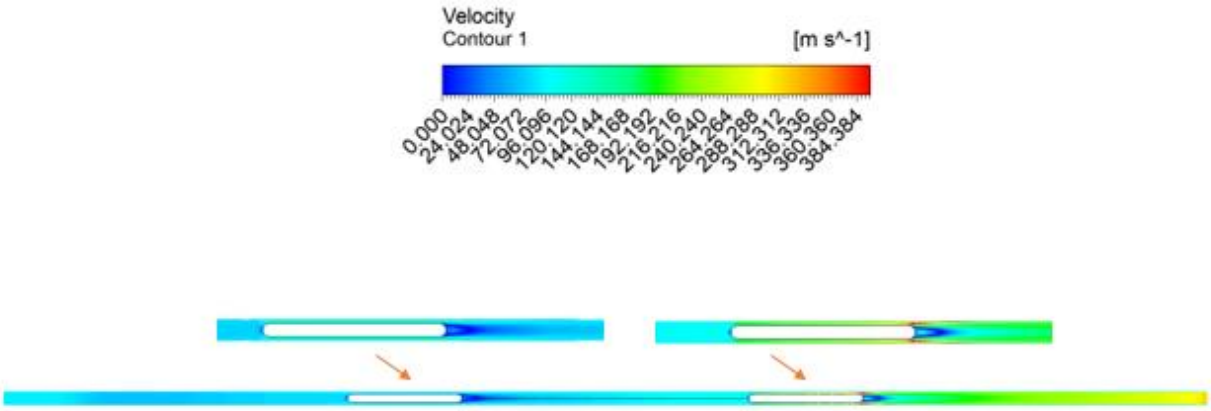

Figure 35: Velocity Distribution around the pods for 100 m/s speed value at the distance of 2.5L between the pods

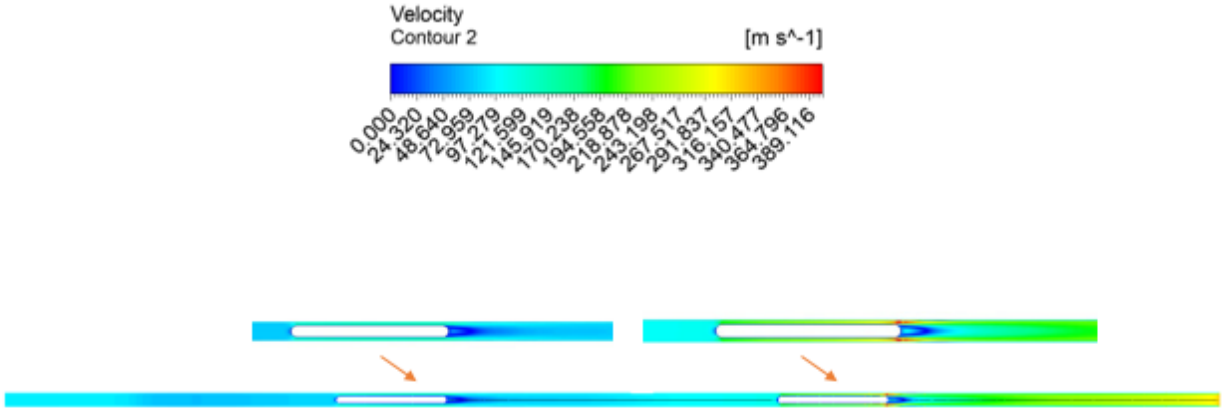

Figure 36: Velocity Distribution around the pods for 100 m/s speed value at the distance of 3L between the pods

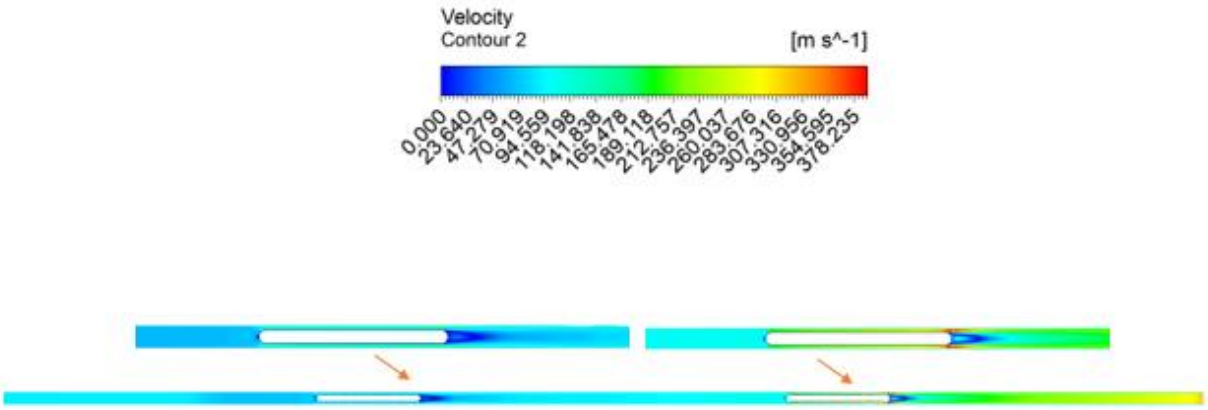

Figure 37: Velocity Distribution around the pods for 100 m/s speed value at the distance of 3.5L between the pods

From Figures 12-30, the pressure of the leading shock wave is increasing with the increase in the speed of the pods. On the contrary, the backward expansion wave generated at the lower end of the second pod generates a low-pressure region in the downstream section. However, a rise in the pressure value exists at the tail section of the first pod as compared to the tail section of the second pod. The rise in the pressure value is large in space between the two pods when the distance between the pods is small i.e., 2L and 2.5L. The rise in the pressure value decreases with the increase in the distance between the pods, as seen in Figures 12-15, 17-20, 22-25, and 27-30. Moreover, the effect of the variation of the backward expansion wave is not as prominent as compared to that of the leading shock wave.

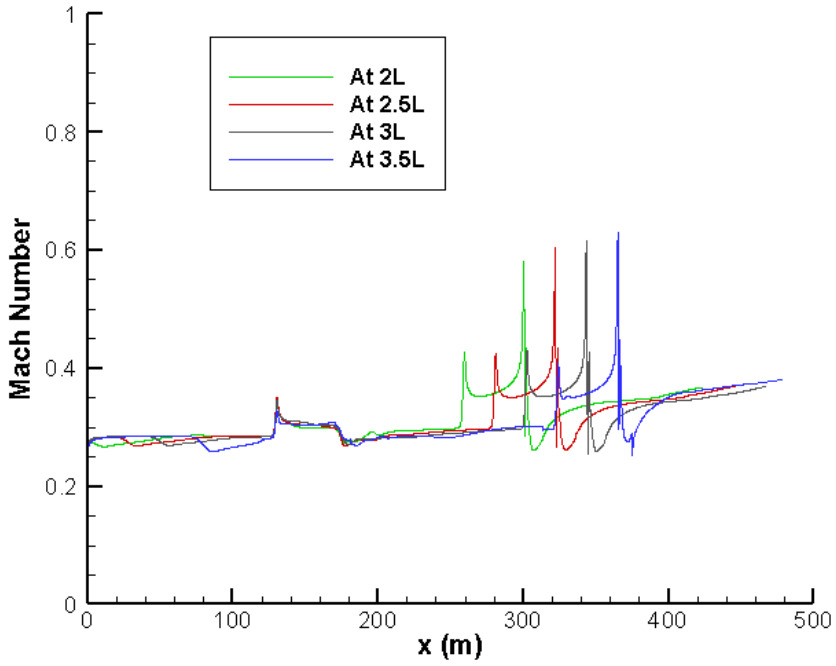

Figure 38: Mach Number variation at 100 m/s flow speed

For the case, when the pod speed is 200 m/s it corresponds to the flow regime 2. An oblique shock wave starts to appear at the divergent section of the pods. The oblique shock wave is more prominent in the case of the second pod as compared to the first pod because the rare end of the second pod does not experience the presence of any other shock wave generated due to the preceding pod. Whereas the rare section (i.e., tail, or divergent section) of the first pod experience the effect of a leading shock wave generated at the head of the second pod. This results in a decrease in the Mach number value at the end of the throat section of the first pod.

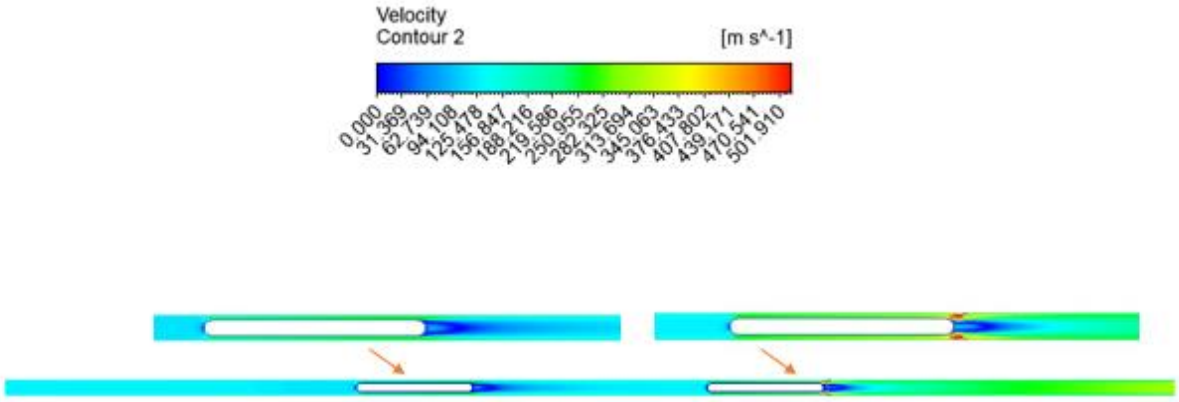

Figure 39: Velocity Distribution around the pods for 200 m/s speed value at the distance of 2L between the pods

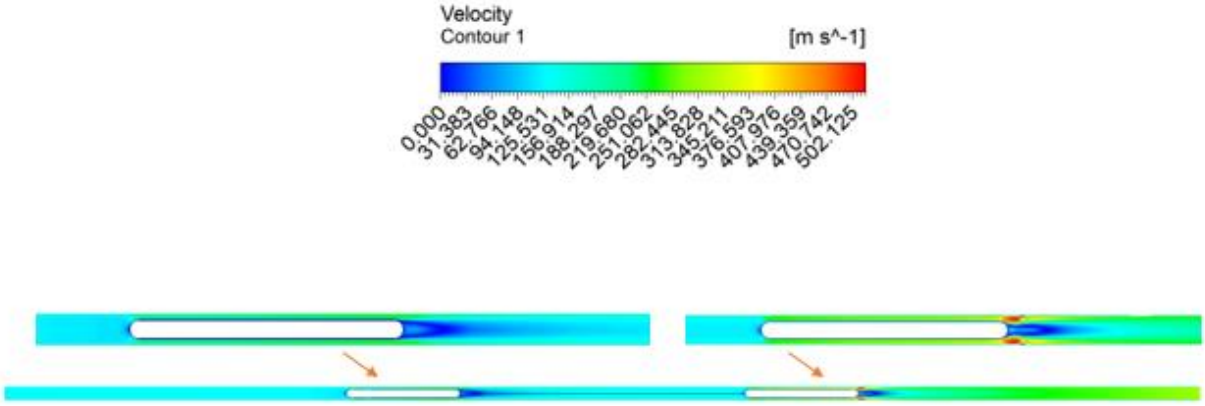

Figure 40: Velocity Distribution around the pods for 200 m/s speed value at the distance of 2.5L between the pods

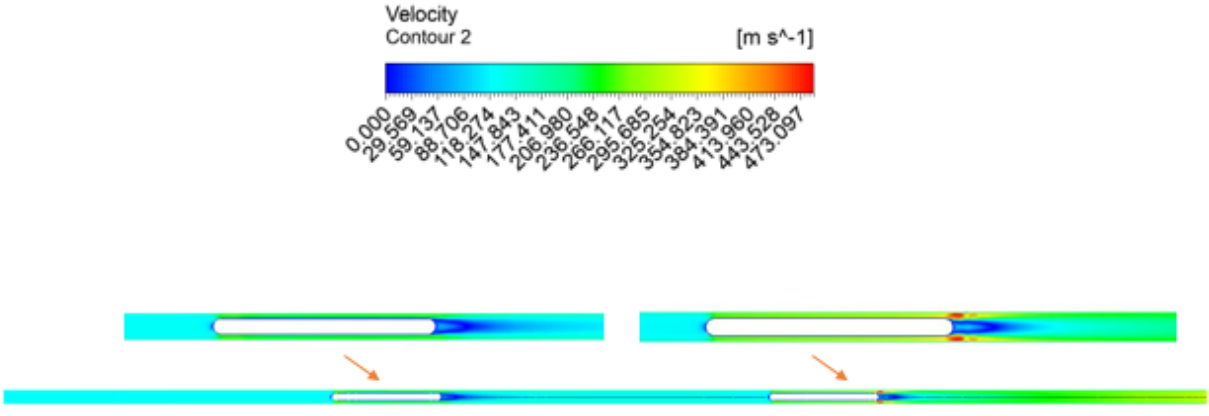

Figure 41: Velocity Distribution around the pods for 200 m/s speed value at the distance of 3L between the pods

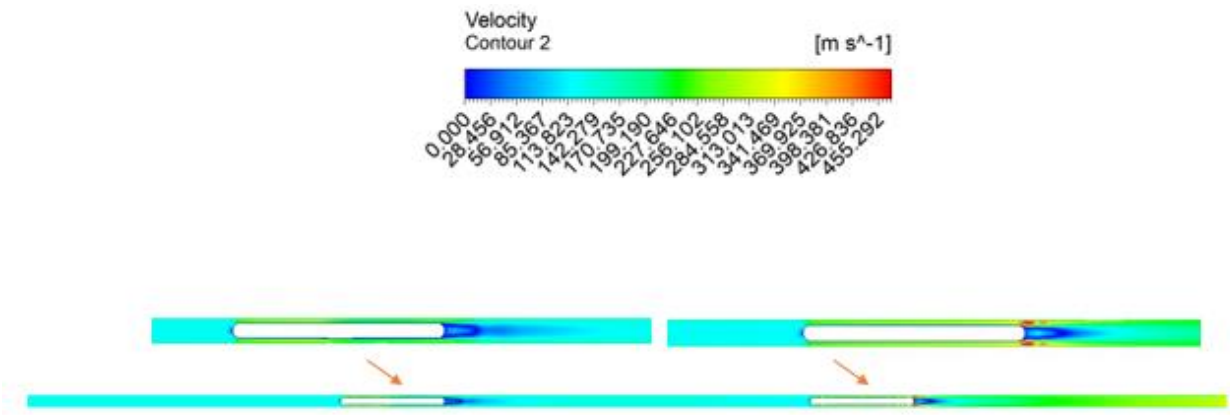

Figure 42: Velocity Distribution around the pods for 200 m/s speed value at the distance of 3.5L between the pods

The chocking exists at the throat section of the second pod in this flow regime. The value of M_{in}^{p} remains smaller for the second pod as compared to $M_{cr,isen}$ due to the existence of boundary layers. Because of the shear field that exists at the wall of the pod and tube, boundary layers are developed along the wall of the pod and tube[16]. Due to these boundary layers, the flow encounters a narrower throat area for the second pod than would otherwise be expected for the designed system. As a result, the real value of the Mach number M_p is lower for the second pod as compared to the critical Mach number $M_{cr,isen}$. Moreover, for the second pod, the maximum value of the Mach number achieved at the throat is lower as compared to the first pod. This is due to the interaction of the low-pressure region (at the tail of the first pod) and high-pressure leading shock wave (at the head of the second pod). However, due to the existence of boundary layers at the throat section of the second pod, a large value of Mach number is observed.

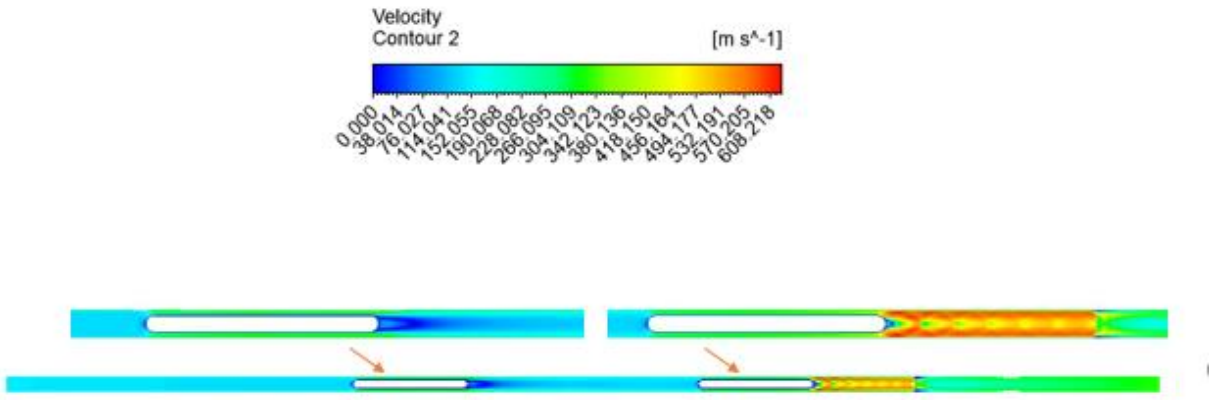

Figure 43: Velocity Distribution around the pods for 300 m/s speed value at the distance of 2L between the pods

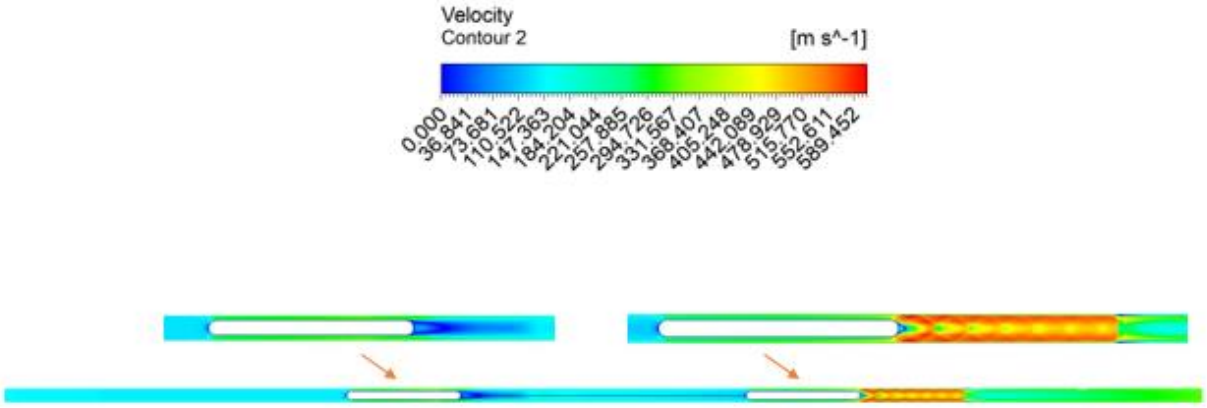

Figure 44: Velocity Distribution around the pods for 300 m/s speed value at the distance of 2.5L between the pods

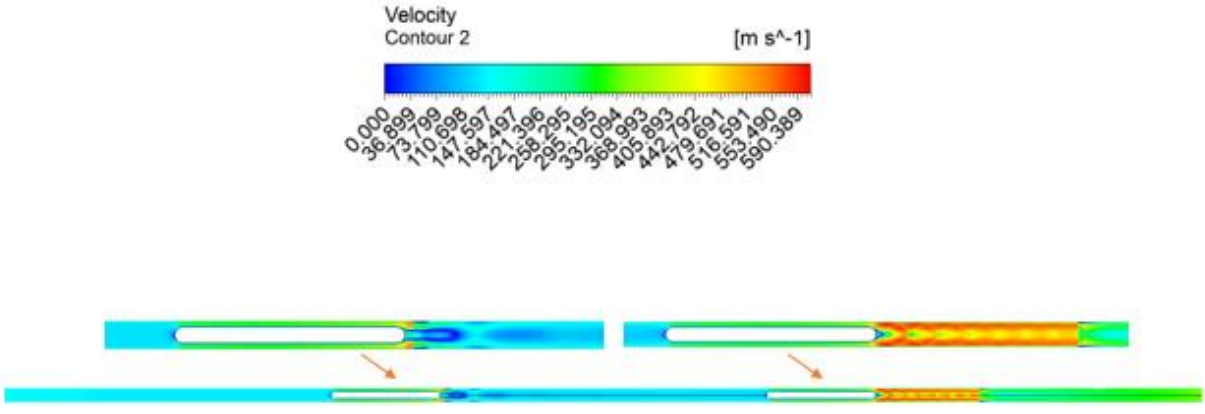

Figure 45: Velocity Distribution around the pods for 300 m/s speed value at the distance of 3L between the pods

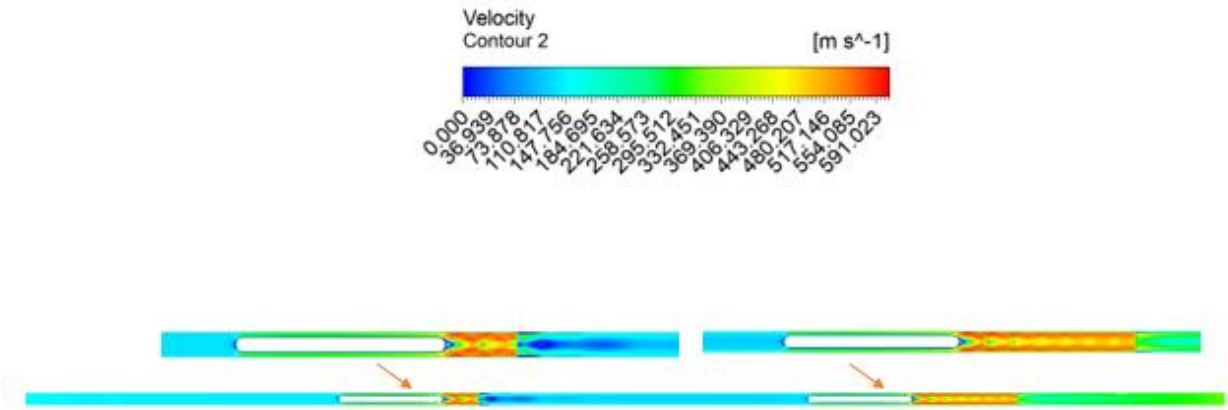

Figure 46: Velocity Distribution around the pods for 300 m/s speed value at the distance of 3.5L between the pods

An oblique shock wave exists at the tail section of the second pod. The oblique shock wave is pushed backwards at a higher value of pod speed, allowing the flow to accelerate further[16] in the divergent section of the second pod. Moreover, the viscosity effect causes a flow separation at the tail of the first pod. As a result, the separation of the flow postpones the divergence of the flow's region of encounter. Due to this, the flow accelerates after the diverging part and continues for a short distance further.

However, the oblique shock wave generated at the tail section of the first pod disappears due to its interaction with the leading shock wave. The trailing oblique shock wave is a lower pressure wave and results in a lower pressure region at the tail of the first pod, whereas the leading shock wave is a high-pressure wave. With a smaller value of the distance between the pods, the trailing oblique shock wave interacts with the leading shock wave, which results in the overall intermediate value of pressure between the two pods. A flow separation region is encountered at the interaction point of the two shock waves. A similar flow separation phenomenon is observed at the tail of the second pod, as a result, the delay in the divergence of the area encountered by the flow is observed, as seen in Figure 47.

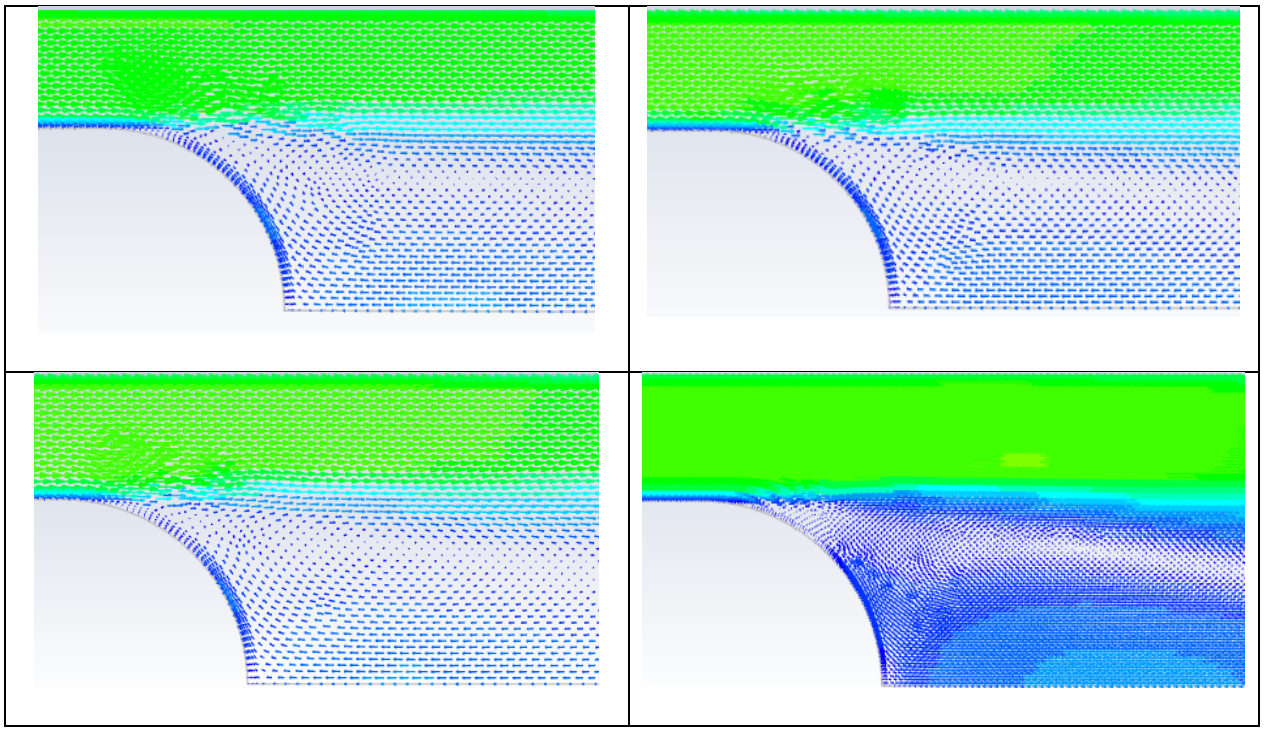

Figure 47: Velocity vector around the tail of the second pod for a pod speed of 200 m/s

Moreover, due to the small value of the distance between the pods (i.e., 2L), the two different pressure regions encounter each other at the tail of the first pod. This results in small pressure fluctuation close to the tail of the first pod, but the overall flow stream remains smooth, and no flow separation is observed in this case.

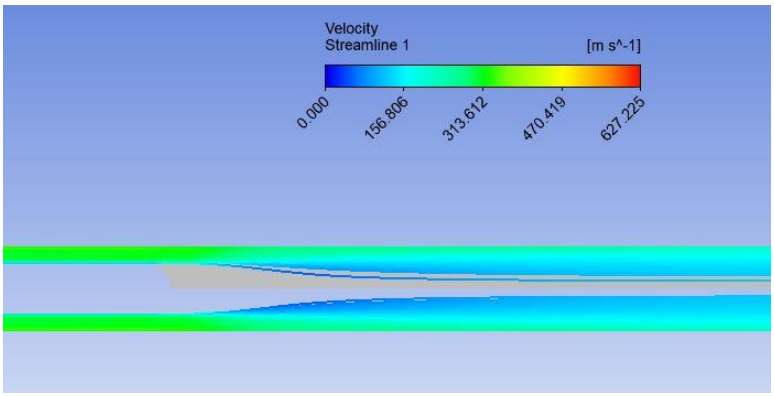

Figure 48: Interaction Region of the Trailing Expansion wave and the Leading Compression Wave at the tail of the first pod at a distance value of 2L for the pod speed of 300 m/s

Apart from the pressure oscillation caused by the oblique shock wave, regime 2's propensity for pressure is comparable to regime 1's, as illustrated in Figure 23. As the pod speed rises, so does the pressure in the LSW, while the pressure in the BEW falls. Finally, with the pod speed increasing, P_{in} rises and P_{ex} falls.

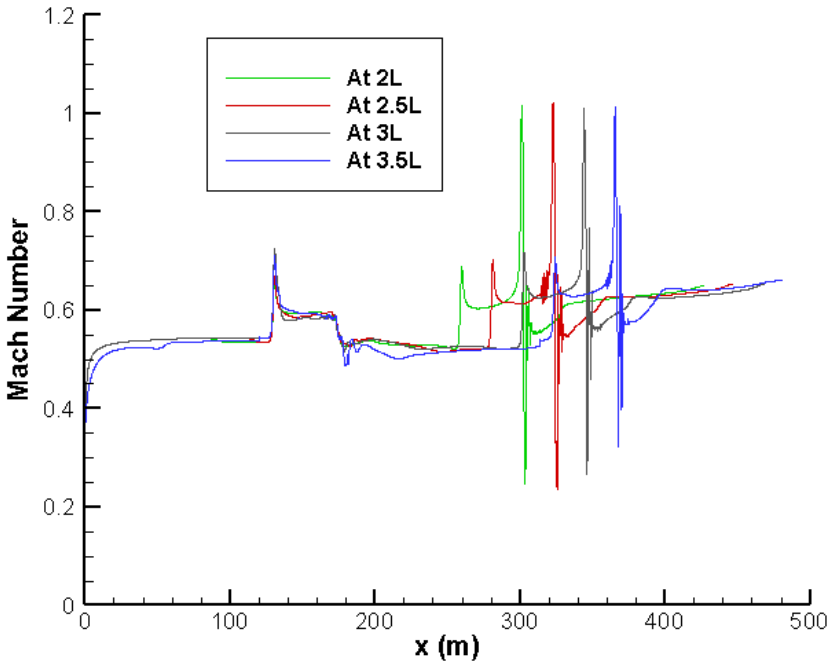

Figure 49: Mach Number variation at 200 m/s flow speed

The flow regime 3 exists for the pod speed of 300 to 400 m/s. At the distance value of 2L to 2.5L between the pods, no jet is observed at the tail of the first pod for the pod speed value of 300 m/s. Similarly, for a distance value of 2L between the pods, no jet formation is observed at the tail section of the first pod at a speed value of 400 m/s of the pods. This is due to the interaction of the low pressure trailing oblique shock wave and the high-pressure leading shock wave due to the smaller distance between the two pods. As a result of this interaction between two pressure waves, the pressure region between the pods is neutralized i.e., it results in a high value of the pressure as seen in Figures 28 and 33. This high value of pressure results in no jet formation at the tail section of the first pod, as seen in Figures 43, 44 and 50.

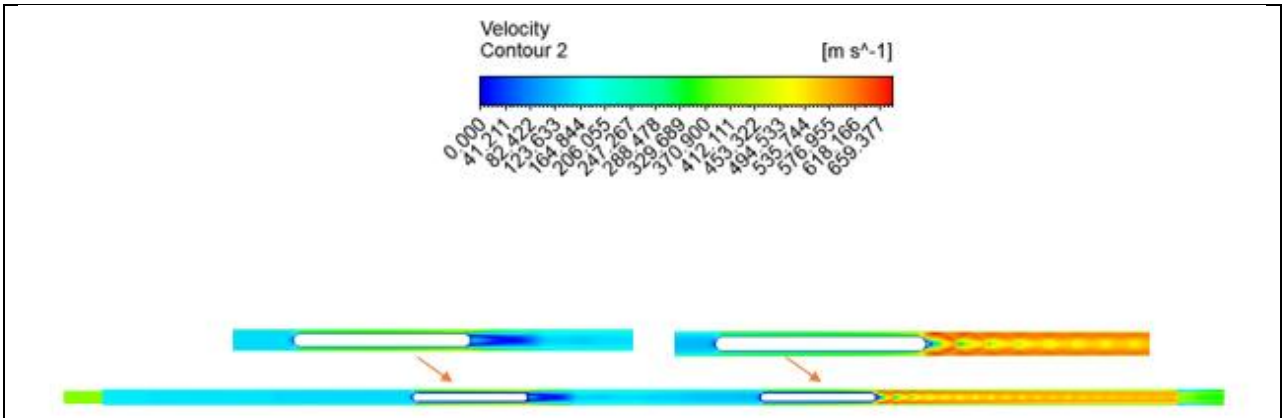

Figure 50: Velocity Distribution around the pods for 400 m/s speed value at the distance of 2L between the pods

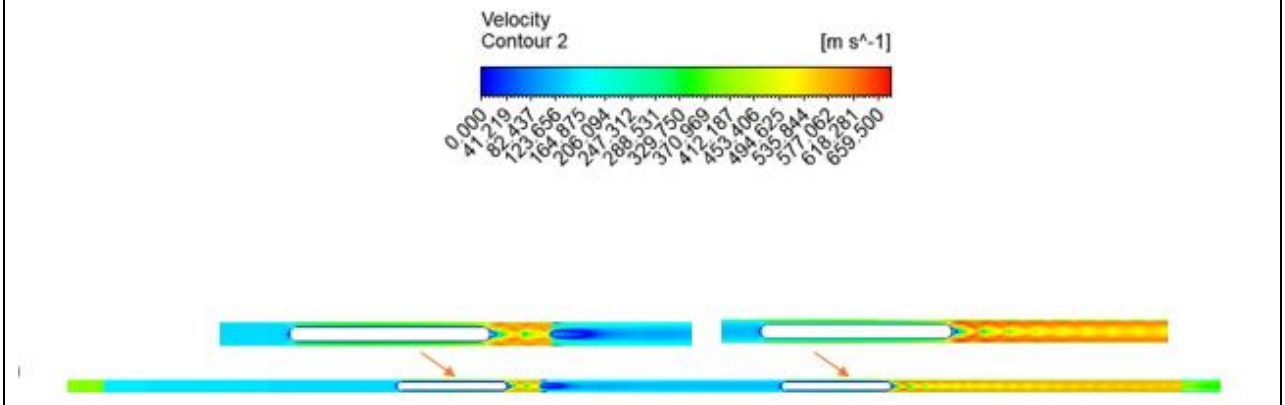

Figure 51: Velocity Distribution around the pods for 400 m/s speed value at the distance of 2.5L between the pods

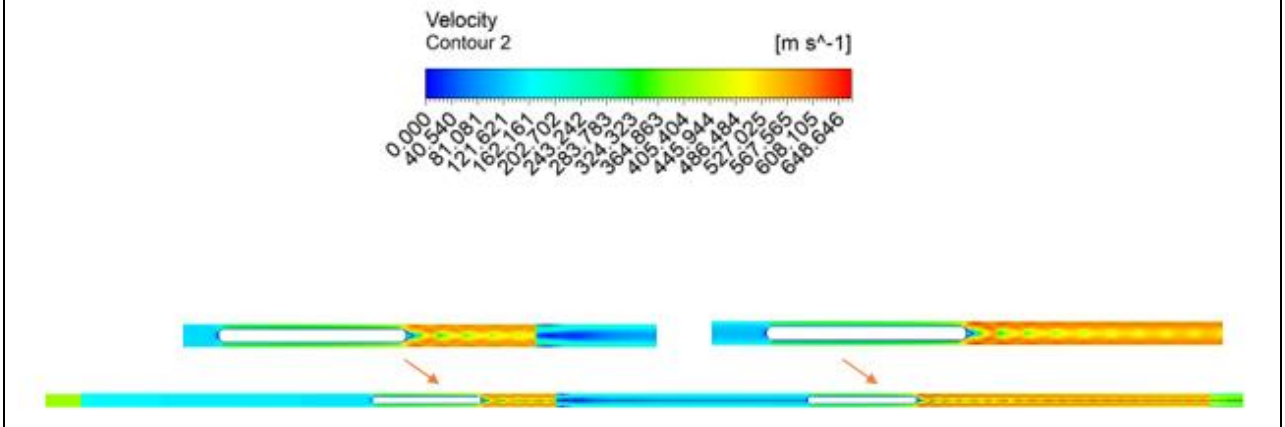

Figure 52: Velocity Distribution around the pods for 400 m/s speed value at the distance of 3L between the pods

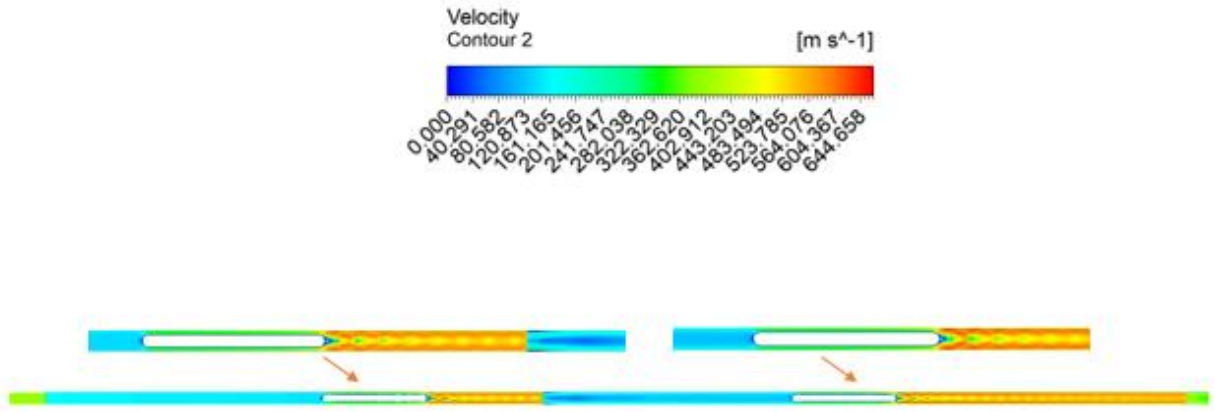

Figure 53: Velocity Distribution around the pods for 400 m/s speed value at the distance of 3.5L between the pods

Additionally, the intense interaction of the expansion wave and the compression wave results in the flow separation phenomenon close to the walls of the tube, as seen in Figure. Moreover, two additional converging-diverging sections are encountered by the flow. A flow separation region is also formed in the middle section of the flow stream due to the viscosity effect of the flow, which leads to the delay in the flow region of the encounter. This results in the expansion of the flow pattern at the later section of the interaction of the two pressure waves, which in turn leads to the decrease in the overall pressure value at the front section of the second pod.

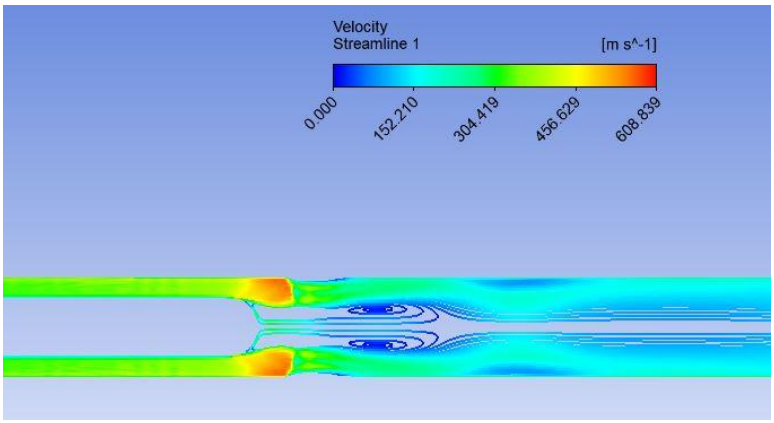

Figure 54: Interaction Region of the Trailing Expansion wave and the Leading Compression Wave at the tail of the first pod at a distance value of 3L for the pod speed of 300 m/s /s

Increasing the speed of the pod results in an increase in the strength of the flow separation phenomenon close to the walls of the tube, as seen in Figure. Moreover, only a single converging-diverging section is encountered by the flow stream. This leads to a decrease in the pressure value as for the case when the distance between the pods was 3L. However, due to the large distance between the pods (i.e., 4L) the pressure value at the frontal section of the second pod is smaller as compared to the previous case. this leads to an overall lower value of pressure drag for the second pod.

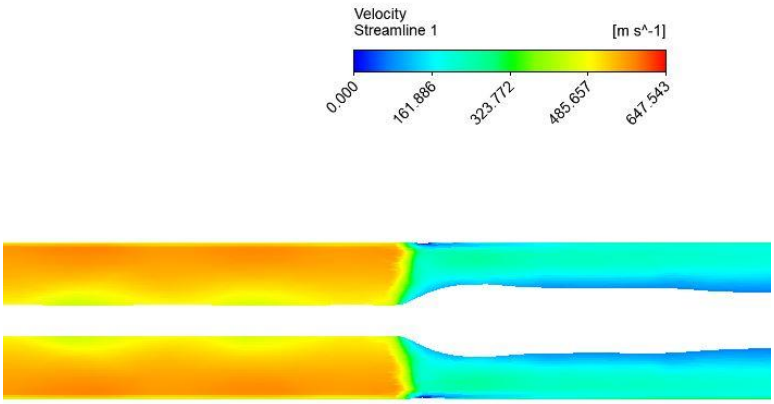

Figure 55: Interaction Region of the Trailing Expansion wave and the Leading Compression Wave at the tail of the first pod at a distance value of 4L for the pod speed of 300 m/s /s

On the other hand, the second pod shows a different kind of behaviour. A low-pressure region exists at the tail end of the second pod. This results in the development of the jet with reduced expansion at the tail of the first pod. An under-expansion results at the tail of the first pod due to the confined space in the case of the Multi-Pod Hyperloop System. A shock cell structure for the first pod is observed in this under the expanded jet. Additionally, due to the reflection at the tube walls, the shock cell structures observed for the second pod vary from the structure found in an under-expanded jet in open space. However, it is comparable to that found for an under-expanded confined jet[47]. Moreover, for the pod's distance of 2L, the Mach number at the tail of the first pod reduces further instead of increasing due to this high value of pressure. The Mach number observed at the tail of the first pod is 0.8. However, with the increase in the distance between the pods the pressure value of the region between the pods reduces due to delay in the pressure waves interaction.

With the increase in the distance between the pods (i.e., 3L to 3.5L), a jet with a reduced expansion is observed at the tail of both pods. This is due to the lower pressure value behind the pods, a lower pressure region is developed which results in a lower value of P_{ex}. As a result of this under expansion, a shock cell structure is observed under the expanded jet. The distribution of Mach numbers in regime 3 is seen in the figure.

In addition, the divergent section of both pods does not include the oblique shock wave, and the flow is completely accelerated through the divergent section. As a result, M_{ex}^{p} stays constant regardless of how fast the pods are moving forward. For a flow that is inviscid and isentropic, and M_{ex}^{p} is 1.91, which is equal to the supersonic solution of Eq (1)[16]. However,

because of the influence of the boundary layer, the flow meets a narrower throat region, and the flow's Mach number jumps to as high as 2.10 for the second pod. The highest Mach number appears significantly distant from the tail of the second pod at this point, as previously discussed for the flow regime 2.

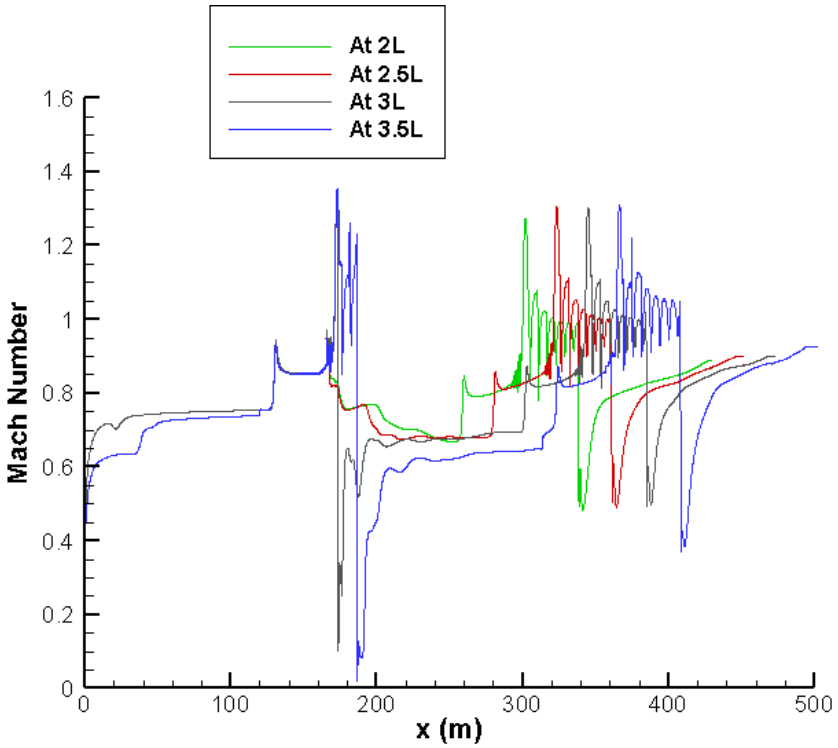

Figure 56: Mach Number variation at 300 m/s flow speed

The flow affinities of the pressure value of leading shock wave, backward expansion wave and p_{in} is just like the flow regime 1 and 2, as seen from the figure. However, the p_{ex} exhibits distinct kinds of behavior concerning the speed of the pod. It is observed that the total pressure value increases with the increase in the pod's speed. The following equation expresses the overall pressure in a compressible flow:

$$P_T = P\left[1 + \left(\frac{\gamma - 1}{2}\right)(M^p)^2\right]^{\frac{\gamma}{\gamma-1}} \tag{19}$$

In this equation, P_T corresponds to the total pressure value. As a result of Eq. (20), it has been found that the pressure rises at a rate that is proportional to that of the increase in total pressure provided that the Mach number is held constant. As a result, under regime 3, P_{ex} grows in proportion to the increase in speed of the pods.

4.5. Analysis of Aerodynamic Drag Distribution:

Figure 57-60 shows the simulated results for the pressure values at the nose and tail of both pods. The p_{tail} for first pod and p_{nose} for the second pod decreases with the increase in the distance between the pods at all values of the speed. There is a large value of pressure at the tail of the first pod and the nose of the second pod at a smaller distance value for all pod speeds. This is because the smaller distance between the pods causes the compression of the particles in between the pod, which results in an intense rise in the pressure value. However, increasing the distance between the pods result in a decrease in the value of p_{tail} for first pod and p_{nose} for the second pod. Increasing the distance between the pods allows the air particles in between the pods to move smoothly in between the pods and hence a decrease in the drag is observed.

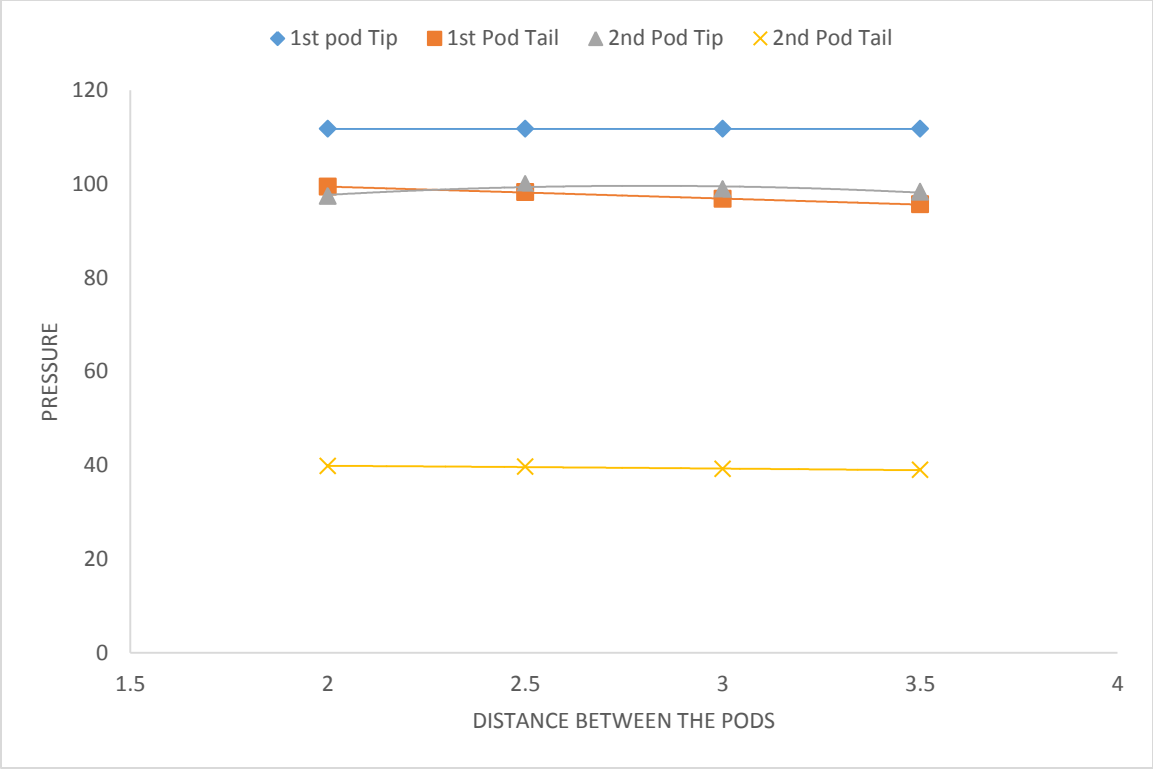

Figure 57: Drag force distribution at the nose and tail of both pods at a flow speed of 100 m/s

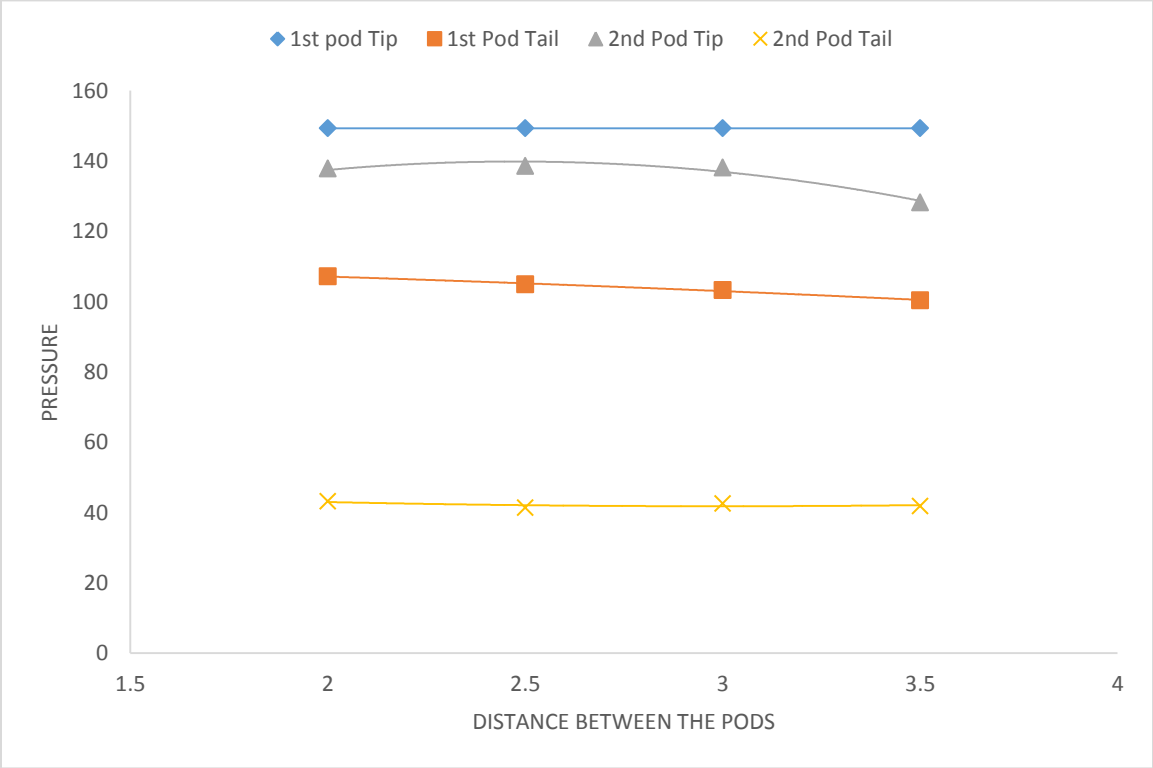

Figure 58: Drag force distribution at the nose and tail of both pods at a flow speed of 200 m/s

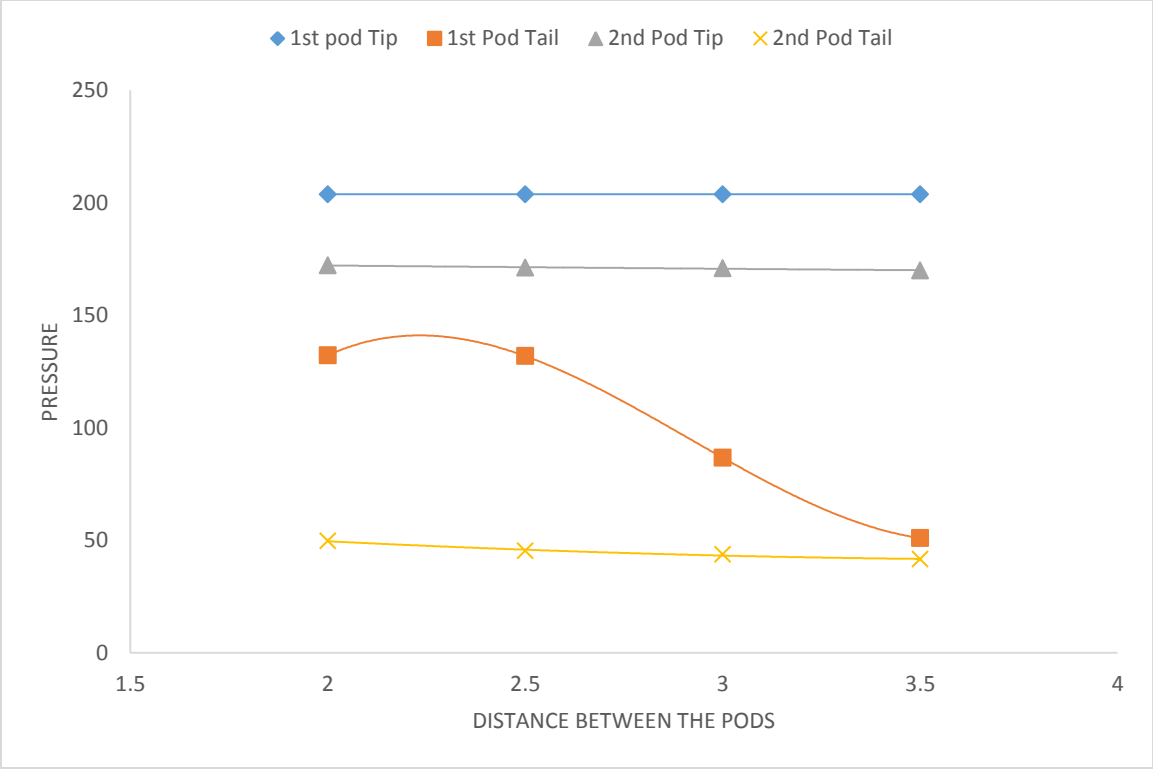

Figure 59: Drag force distribution at the nose and tail of both pods at a flow speed of 300 m/s

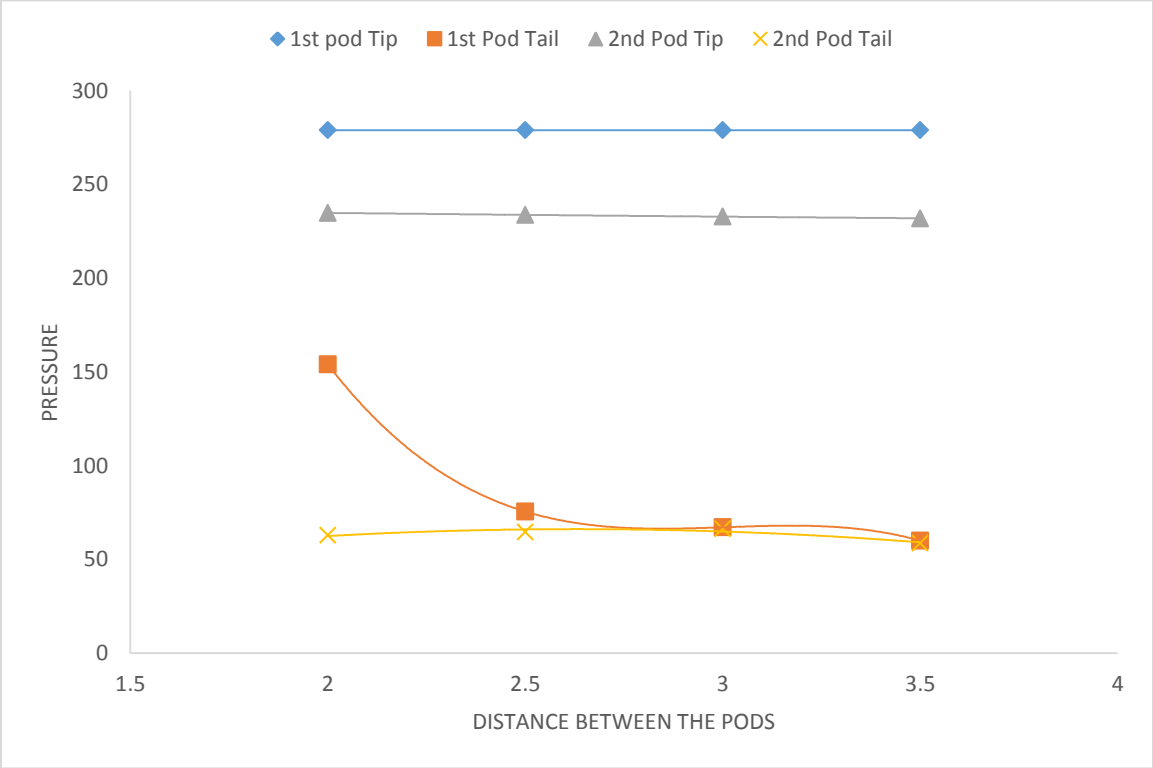

Figure 60: Drag force distribution at the nose and tail of both pods at a flow speed of 400 m/s

The value of drag force increases with the increase in the speed of the pods. Moreover, at all values of pod speed, increasing the distance between the pods also results in a decrease in the value of the drag force on the pods. The pressure value observed at the tail of the pods also increases with the increase in the pod speed, flow regime 3, whereas, the $\bar{p}_{tail}$ decreases in regimes 1 and 2. Because of this rise in the $\bar{p}_{tail}$ value, the decrease in the drag value in flow regime 3 is lower as compared to flow regimes 1 and 2.

4.6. Temperature Distribution:

Another important parameter that is affected by the shock wave interaction is the temperature distribution along the walls of the tube. The results of the simulation suggest that, when the distance between the pods is small, a maximum rise in the temperature is achieved at the point of interaction of oblique shock wave, normal shock wave and the boundary layer. A separation in the boundary layers exists at the tail section of the first pod where the interaction of the oblique shock wave and the normal shock wave happens, as seen in Figure 61. This is due to the intense pressure and temperature gradient at the tail end of the first pod. However, increasing the distance between the pods decreases the intensity of the shock waves interaction, as a result, the maximum temperature value reached is decreased.

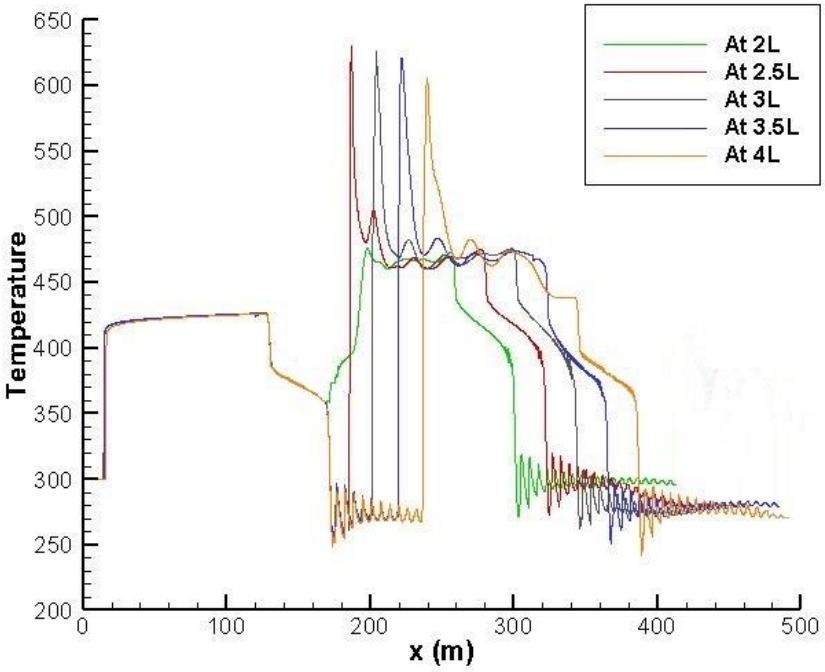

Figure 61: Temperature Distribution at a speed value of 400 m/s

Chapter No. 5

This chapter provides the conclusion to the analysis and the main objectives that were achieved through this research work. Moreover, the limitation of the current model and the recommendation that will prove to be helpful in the future are also described in this chapter.

5. Conclusion:

The behaviour of the flow regime and the pressure waves interaction was analyzed for the different values of distances between the pods of the multi-pod hyperloop system using the 2D, axisymmetric, unsteady-state simulation, moreover, a comparison of the numerical model results was also made to the theoretical quasi-one-dimensional approach. Based on the compressible flow phenomenon the flow around the pod is divided into three different flow regimes based on the speed of the pods. The behaviour of the leading shock wave, the trailing oblique shock wave and the expansion wave was analyzed for all these flow regimes. Based on the confined configuration of the tube the compression wave was also analyzed for flow regime 1 even though the flow is subsonic for this case. The oblique shock wave starts to develop at the tail section of the second pod for the flow regime 2, however, the flow phenomenon is different at the tail section of the first pod. the trailing shock wave appears for both pods in the case of the flow regime 3. Due to the existence of the compression waves, the leading shock waves, the trailing shock waves, and the expansion waves, the distance between the pods of the multi-pod hyperloop system becomes an important parameter for the determination of aerodynamic characteristics of the Multi-pod Hyperloop System.

The shock waves play a significant role in the determination of the aerodynamic characteristics of the multi-Pod Hyperloop system. Moreover, the distance between the pods is another crucial factor that affects the flow regime between the pods of the Multi-Pod Hyperloop System. Based on this study, it is observed that chocking of the flow is affected by the existence of the leading shock wave as well as by the boundary layer for both pods, and as the distance between the pods increases the pressure decreases at the tail section of the first pod and at the

head section of the second pod which results into overall decrease in the drag force value for both pods, as seen from Figure 57-59.

For flow regime 1, drag force is exceptionally large when the distance between the pods is small i.e., 2L to 3L. The space between the two pods is not large enough for the compression wave from the second wave to travel. The strong compression wave remains confined between the two pods which results in the high-pressure value between the two pods i.e., at the tail end of the first pod and the head section of the second pod. Increasing the distance between the pods i.e., 3L to 4L provides sufficient space for the compression wave to travel and hence does not affect the flow field around the first pod. Hence, a decrease in the drag force is observed.

For flow regime 2, no chocking is observed for the first pods due to the pressure wave interaction between the two pods. However, chocking of the flow happens for the second pod due to the boundary layer separation. Oblique shock wave starts to develop for the second pod in this flow regime. Development of the OSW results in the high value of pressure drag for the second pod. Moreover, a large pressure value is observed at the tail end of the first pod, when the distance between the pods is small (i.e., 2L to 3L) due to confinement of the space, which results in the high value of drag for the pod. Increasing the distance between the pods i.e., 3L to 4L results in a decrease in the drag force due to the delay in the pressure waves' interaction, as seen in Figure 58.

For flow regime 3 (i.e., at 300 m/s and 400 m/s), no OSW is observed at the tail section of the first pod at the distance value of 2L to 3L at 300 m/s and the distance value of 2L at 400 m/s. The strong compression waves and the limited space between the pod is the reason for the high-pressure region between the two pods at these distances. Moreover, a large value of drag force is observed in these cases. Increasing the distance between the pods i.e., from 3L to 4L at 300 m/s

and from 2.5L to 4L results in the development of the boundary layer separation at the tail end of the first pod which plays a vital role in the development of the oblique shock wave and flow acceleration phenomenon. The drag force decreases rapidly due to the increase in the strength of the oblique shock wave, as seen in Figures 58, and 59. Moreover, when the distance between the pods is small, a flow separation region is formed at the interaction point of the leading shock wave from the second pod and the trailing expansion wave from the first pod. This results in the development of multiple converging-diverging sections of the flow field close to the tail of the first pod. Increasing the distance between the pods results in a decrease in the intensity of the flow separation phenomenon by delaying it.

In this study, the distance between the pods and their effect on the flow field as well as on the aerodynamic characteristics for different flow regimes are studied for the Multi-Pod Hyperloop System. The results of this analysis will help in the design of the multi-Pod Hyperloop system by providing an understanding of the compressible flow phenomenon and how it is affected by the distance between the multiple pods inside the tube.

6. Limitation:

In this research work, the shape of the pods and the tube used are the most idealized ones to study the general mechanics of the flow interaction around the pods. Moreover, the analysis performed was a two-dimensional, axisymmetric analysis which results in one of the most simplified analyses of the aerodynamic characteristics of the pods. Moreover, the theoretical consideration for the equation (13) and (19) are derived from the idealized shape of the pods. It was also assumed that the throat section of the pod would experience a choking phenomenon through the diverging section under the completely accelerated flow conditions.

7. Future Recommendations:

The above-mentioned findings will make a significant contribution to the future development of the multi-Pod Hyperloop pods Based upon the results of the simulation; the following improvements might help to improve the quality of the results.

The aerodynamic solver can be improved by extending its capabilities. Focusing on boundary layer development may have a major impact on the solver's accuracy since it is so critical to velocity distribution and hence flow parameters of interest distribution. A more precise transition location (or the Re relevant to these situations and geometries in that respect) might already lead to significant solver improvements. Improved solver accuracy may be advantageous to the optimization process as greater accuracy can be obtained if the total solver accuracy is raised. This is especially true for distributional trends.

The solution disregards structural, economic, infrastructural, and performance constraints. Without a question, they are all critical parts of the Hyperloop's system design. These are, without a doubt, critical features of the Hyperloop's System. A final detailed pod design will therefore need to integrate these considerations for future work to better define physical constraints. The aerodynamic solver may be included in a wider multidisciplinary design optimization framework considering these observations.

The accuracy of the results can be improved further by implementing a more complex and realistic pod and tube shape. Moreover, the theoretical assumptions for equations (13) and (19) are appropriate since the Hyperloop system in our case is intended to travel at transonic speeds. Additionally, the distinction between theoretical results and simulation is shown by the absence

of consideration of the boundary layer in the consideration of the theoretical equations. As a result, using the boundary layer in the theoretical calculation may increase results accuracy in the future.

Moreover, in future studies, three-dimensional unsteady state simulations should be conducted to better understand the propagation of the compression waves and the interaction of the oblique shock wave and the normal shock wave (compression wave). Additionally, the design of the pod employed in future work should be more complex and under more realistic conditions will help to optimize the distance between the pods and hence, it will help to decrease the aerodynamic drag on the pods.

References:

1. Schafer, A., D.G.J.T.r.p.a.p. Victor, and practice, *The future mobility of the world population.* 2000. **34**(3): p. 171-205.
2. Pierce, A.J.T.D., *Hyperloop-A New Transportation System.* 2017. **76**(9): p. 8.
3. Aggarwal, A., K. Bajaj, and S.J.I.-A.I.J.o.J.N.U. Shiwani, *Hyperloop: The Future of Transportation.* 2018. **7**(1and2): p. 30-34.
4. Musk, E.J.S.H., CA, USA, *Hyperloop alpha.* 2013.
5. Janić, M.J.T.P. and Technology, *Future advanced long-haul Evacuated Tube Transport (EET) system operated by TransRapid Maglev (TRM): a multidimensional examination of performance.* 2019. **42**(2): p. 130-151.
6. Le, T.T.G., et al., *Numerical investigation of aerodynamic drag and pressure waves in hyperloop systems.* 2020. **8**(11): p. 1973.
7. Oh, J.-S., et al., *Numerical analysis of aerodynamic characteristics of hyperloop system.* 2019. **12**(3): p. 518.
8. Palacin, R.J.I.E.M., *Hyperloop, the electrification of mobility, and the future of rail travel.* 2016. **4**(3): p. 4-51.
9. Davies, K., et al. *A review of Turboelectric Distributed Propulsion technologies for N+ 3 aircraft electrical systems*. in *2013 48th International Universities' Power Engineering Conference (UPEC)*. 2013. IEEE.
10. Van Driest, E.R., *The problem of aerodynamic heating*. 1956: Institute of the Aeronautical Sciences.
11. Baron, A., et al., *The alleviation of the aerodynamic drag and wave effects of high-speed trains in very long tunnels.* 2001. **89**(5): p. 365-401.

12. Niu, J., et al., *Numerical study on the impact of Mach number on the coupling effect of aerodynamic heating and aerodynamic pressure caused by a tube train.* 2019. **190**: p. 100-111.

13. Zhou, P., et al., *Numerical study on wave phenomena produced by the super high-speed evacuated tube maglev train.* 2019. **190**: p. 61-70.

14. Yang, Y., et al. *Aerodynamic simulation of high-speed capsule in the Hyperloop system*. in *35th AIAA applied aerodynamics conference*. 2017.

15. Hruschka, R. and D.J.S.W. Klatt, *In-pipe aerodynamic characteristics of a projectile in comparison with free flight for transonic Mach numbers.* 2019. **29**(2): p. 297-306.

16. Jang, K.S., et al., *Effects of compressible flow phenomena on aerodynamic characteristics in Hyperloop system.* 2021. **117**: p. 106970.

17. Gillani, S., et al., *CFD analysis of aerodynamic drag effects on vacuum tube trains.* 2019. **12**(1): p. 303-309.

18. Bibin, S. and S.K. Mukherjea. *Numerical investigation of aerodynamic drag on vacuum tube high speed train*. in *ASME International Mechanical Engineering Congress and Exposition*. 2013. American Society of Mechanical Engineers.

19. Kang, H., et al., *A study on the aerodynamic drag of transonic vehicle in evacuated tube using computational fluid dynamics.* 2017. **18**(4): p. 614-622.

20. Zhang, Y.J.J.o.M.T., *Numerical simulation and analysis of aerodynamic drag on a subsonic train in evacuated tube transportation.* 2012. **20**(1): p. 44-48.

21. Zhou, P., J. Zhang, and T.J.I.J.o.R.T. Li, *Effects of blocking ratio and Mach number on aerodynamic characteristics of the evacuated tube train.* 2020. **8**(1): p. 27-44.

22. Wong, F., *Aerodynamic design and optimization of a hyperloop vehicle.* 2018.

23. Bao, S., et al., *Numerical study on the influence of initial ambient temperature on the aerodynamic heating in the tube train system.* 2020. **2**(1): p. 1-18.

24. Kim, T.-K., et al., *Aerodynamic characteristics of a tube train.* 2011. **99**(12): p. 1187-1196.

25. Sui, Y., et al., *An aerothermal study of influence of blockage ratio on a supersonic tube train system.* 2020: p. 1-12.

26. Jiqiang, N., et al., *Effect of acceleration and deceleration of a capsule train running at transonic speed on the flow and heat transfer in the tube.* 2020. **105**: p. 105977.

27. Yuangui, M., et al., *Numerical research on basic characteristics of tunnel entry waves induced by a high-speed train running into the tunnel.* 2015. **33**(5): p. 686-696.

28. Bizzozero, M., et al., *Aerodynamic study of a Hyperloop pod equipped with compressor to overcome the Kantrowitz limit.* 2021. **218**: p. 104784.

29. Bi, H. and B. Lei. *Aerodynamic characteristics of evacuated tube high-speed train*. in *International Conference on Transportation Engineering 2009*. 2009.

30. Maicke, B.A., et al., *Characterization of the startup and pressure blowdown processes in rocket nozzles.* 2013. **25**(1): p. 273-282.

31. Maicke, B.A., G.J.A.S. Bondarev, and Technology, *Quasi-one-dimensional modeling of pressure effects in supersonic nozzles.* 2017. **70**: p. 161-169.

32. Pritchard, P.J., *Introduction to Fluid Mechanics 8th Edition. Fox and McDonald*. 2011, Wiley.

33. Zhou, C., et al., *Numerical investigation on the aerodynamic performance and flow mechanism of a fan with a partial-height booster rotor.* 2021. **109**: p. 106411.

34. Menter, F. *Zonal two equation kw turbulence models for aerodynamic flows*. in *23rd fluid dynamics, plasmadynamics, and lasers conference*. 1993.

35. Hasan, R. and J.J.T.A.J. McGuirk, *Assessment of turbulence model performance for transonic flow over an axisymmetric bump.* 2001. **105**(1043): p. 17-32.

36. https://knowledge.autodesk.com. *SST K-Omega Turbulence Models*. 2022 [cited 2022 5/19/2022]; Available from: https://knowledge.autodesk.com/support/cfd/learn-explore/caas/CloudHelp/cloudhelp/2014/ENU/SimCFD/files/GUID-0F5C4828-9F91-46B6-A16A-2578D72DCFCC-htm.html.

37. Fujio, C., et al., *Numerical investigation of axisymmetric intake flowfield and performance for scramjet-powered ascent flight.* 2021. **111**: p. 106531.

38. Balabel, A., et al., *Assessment of turbulence modeling for gas flow in two-dimensional convergent–divergent rocket nozzle.* 2011. **35**(7): p. 3408-3422.

39. Chen, X., et al., *Aerodynamic simulation of evacuated tube maglev trains with different streamlined designs.* 2012. **20**(2): p. 115-120.

40. Braun, J., J. Sousa, and C.J.A.J. Pekardan, *Aerodynamic design and analysis of the hyperloop.* 2017. **55**(12): p. 4053-4060.

41. Opgenoord, M.M. and P.C.J.A.J. Caplan, *Aerodynamic design of the Hyperloop concept.* 2018. **56**(11): p. 4261-4270.

42. Hermes, V., et al., *Numerical investigation of unsteady wave phenomena for transonic airfoil flow.* 2013. **25**(1): p. 224-233.

43. Garcia-Gutierrez, A., et al., *Aerodynamic optimization of propellers for high altitude pseudo-satellites.* 2020. **96**: p. 105562.

44. Yu, K., et al., *Optimization and analysis of inverse design method of maximum thrust scramjet nozzles.* 2020. **105**: p. 105948.

45. Wang, Y., et al., *Computational study of axisymmetric divergent bypass dual throat nozzle.* 2019. **86**: p. 177-190.

46. Reise, S.P. and N.G.J.A.r.o.c.p. Waller, *Item response theory and clinical measurement.* 2009. **5**: p. 27-48.

47. Ryu, J. and D.J.J.o.F.M. Livescu, *Turbulence structure behind the shock in canonical shock–vortical turbulence interaction.* 2014. **756**.

48. Gageik, M., et al., *Pressure wave damping in transonic airfoil flow by means of micro vortex generators.* 2018. **81**: p. 65-77.

49. Ryu, J., et al., *Study of supersonic wave components in high-speed turbulent jets using an LES database.* 2014. **333**(25): p. 6900-6923.

50. Zebiri, B., et al., *Analysis of shock-wave unsteadiness in conical supersonic nozzles.* 2020. **105**: p. 106060.

51. Anderson, J.D., *Modern compressible flow: with historical perspective*. Vol. 12. 1990: McGraw-Hill New York.

52. Babinsky, H. and J.K. Harvey, *Shock wave-boundary-layer interactions*. Vol. 32. 2011: Cambridge University Press.

Appendix:

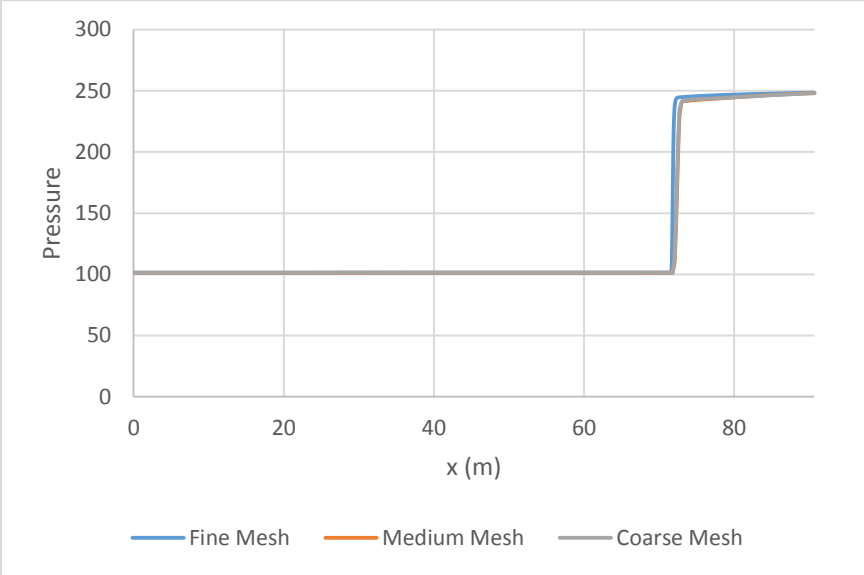

Figure 62: Mesh Independence Test